



UNIVERSITÀ DEGLI STUDI DI TRIESTE
XXXI CICLO DEL DOTTORATO DI RICERCA IN FISICA

A Structural and Optical Insight on Ge-Sb-Te based Nano-composites

Settore scientifico-disciplinare: FIS-03

DOTTORANDA:

Barbara Casarin

COORDINATORE:

Prof. Livio Lanceri

SUPERVISORE:

Prof. Fulvio Parmigiani

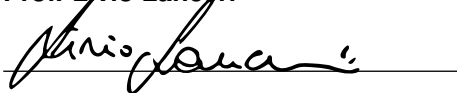
CO-SUPERVISORE:

Dr. Marco Malvestuto

ANNO ACCADEMICO 2017/2018

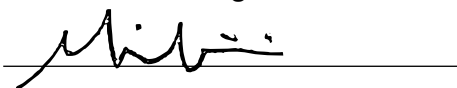
COORDINATORE:

Prof. Livio Lanceri



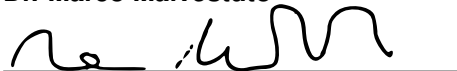
SUPERVISORE:

Prof. Fulvio Parmigiani



CO-SUPERVISORE:

Dr. Marco Malvestuto



Barbara Casarin: *PhD Thesis*, 15th February 2019.

E-MAIL: barbara.casarin@phd.units.it

To my family and Manuel

"With every mistake, we must surely be learning."

The Beatles

CONTENTS

| | | |
|-------|---|----|
| 1 | GENERAL INTRODUCTION | 1 |
| 1.1 | Phase-Change Materials | 3 |
| 1.1.1 | History and Functioning | 3 |
| 1.1.2 | Requirements and Main Composition | 4 |
| 1.1.3 | Atomic Structure: Crystalline and Amorphous Phase | 6 |
| 1.2 | Ge-Sb-Te Nanostructures | 7 |
| 1.2.1 | 2-D: Thin Films and Superlattice Structures | 8 |
| 1.2.2 | 1-D: Nanowires | 9 |
| 1.2.3 | 0-D: Nanoparticles | 10 |
| 1.3 | Thesis Motivation and Outline | 10 |
| 2 | EXPERIMENTAL METHODS | 17 |
| 2.1 | X-Ray Absorption Fine Structure | 19 |
| 2.1.1 | Basic Principles | 19 |
| 2.1.2 | Data Collection and Reduction | 22 |
| 2.1.3 | Data Analysis | 24 |
| 2.2 | Ultrafast Experimental Apparatus | 24 |
| 2.2.1 | The Laser Source | 24 |
| 2.2.2 | The Optical Setup | 25 |
| 3 | LOCAL STRUCTURE OF GST SUPERLATTICES | 31 |
| 3.1 | Recent Advances | 33 |
| 3.2 | Materials and Experimental | 34 |
| 3.3 | Results and Discussion | 35 |
| 3.3.1 | Data | 35 |
| 3.3.2 | TEM Model Structure | 36 |

| | | |
|-------|---|----|
| 3.3.3 | Simulations | 37 |
| 3.3.4 | Wavelet Analysis | 41 |
| 3.3.5 | Fitting Procedure | 43 |
| 3.4 | Conclusions | 46 |
| 4 | SINGLE-SHOT AMORPHIZATION OF GST NANOPARTICLES | 53 |
| 4.1 | Recent Advances and Main Context | 55 |
| 4.2 | Sample Details | 55 |
| 4.3 | Experimental Results | 56 |
| 4.3.1 | Thermodynamics | 60 |
| 4.3.2 | Quantum-Confinement Effects | 63 |
| 4.3.3 | Static Transmittivity | 64 |
| 4.3.4 | X-Ray Diffraction | 68 |
| 4.3.5 | Comparison with Thin Films | 70 |
| 4.4 | Conclusions | 72 |
| 5 | TIME-RESOLVED TRANSMITTIVITY OF GST NANOPARTICLES | 77 |
| 5.1 | Introduction | 79 |
| 5.2 | Experimental Results | 80 |
| 5.2.1 | Data Simulation | 81 |
| 5.2.2 | Fitting Procedure | 83 |
| 5.3 | Discussion | 84 |
| 5.4 | Conclusions | 87 |

ABSTRACT

Electronic memory and computing devices currently rules our digital lives, creating and consuming more than 10^{21} bytes of data per year. This amount is expected to grow exponentially, questing for a so-called “hardware revolution”. Bit size-reduction governed the development of solid-state-memory and semiconductor technologies in the last decades. Yet, the innovative concept of an “universal memory” emerged for transcending the size-node. Indeed, this novel system combines high-speed computation and high-density storage skills. Memory devices based on Phase-Change Materials (PCMs) may serve to the scope, defying to scale reduction and both having a competitive erase/read speed with respect to the primary memory systems -as Static/Dynamic Random Access Memory (SRAM, DRAM)- and the large capacity of non-volatile secondary/tertiary storage systems -as Solid State Disk (SSD), Hard Disk Drive (HDD), Digital Video Disc (DVD).

The appeal of Phase-Change Materials arises from their ability to rapidly and reversibly switch between the amorphous and crystalline states, via optical or electrical pulses. Interestingly, the two structural phases own significantly different physical properties, in particular in terms of reflectivity and conductivity. Many binary or ternary compounds display phase-change features, still Ge-Sb-Te (GST) alloys are the prominent members of this class of materials and are largely employed in industry. However, the main drawback is the PCMs relatively high operation power consumption, in the form of energy required for the phase transformation and of energy dissipation through -primarily- thermal diffusion.

This thesis follows a GST dimensional strategy for power optimization -while maintaining advanced performances- for future integration in novel memory devices. The followed approach includes the case of 2-D highly-textured superlattice structures -of alternately deposited GeTe bilayers and Sb_2Te_3 quintuple layers- and of 0-D $\text{Ge}_2\text{Sb}_2\text{Te}_5$

nanoparticles.

Chapter 1 reviews the state-of-the-art of Phase-Change Materials, that stimulated the research questions addressed in the present work.

Extended X-Ray Absorption Spectroscopy (EXAFS) -briefly presented in the first part of Chapter 2- is a powerful experimental tool for investigating a material's atomic structure. As described in Chapter 3, one of the two allotrope crystalline phases of (GeTe)-(Sb₂Te₃) superlattices is revealed in details via EXAFS measurements performed at the Ge and Sb K-edges. The emerged structural picture is commented in light of the proposed models in literature, advising a power-saving yet over-simplified switching process occurring in the superlattice structure.

Chapter 4 tackles the problem of power consumption by experimentally demonstrating the energy boost on the optical phase-change process occurring in 0-D Ge₂Sb₂Te₅ nanoparticles. Here, a stable but reversible transition from the crystalline to the amorphous state of nanoparticles is induced with a single low-fluence femtosecond laser pulse. Thermodynamic, optical and structural considerations corroborate the experimental evidence.

The laser source together with the setup used for the optical measurements are described in the second part of Chapter 2. The optical arrangement -conceived for time-resolved measurements- led to follow also the relaxation pathways of photo-excited nanoparticles below the threshold fluence for permanent amorphization. The results of this study are unveiled in Chapter 5. The ultrafast dynamics are compared to theoretical simulation and modelled with a phenomenological rate equation. Remarks on the resulting time-scales and the underlying interaction mechanisms -questioning the nature of the resonant bonding- close the Chapter.

SOMMARIO

Le memorie elettroniche e i dispositivi informatici attualmente controllano le nostre vite digitali, creando e consumando più di 10^{21} bytes di dati all'anno. Questa quantità è destinata a crescere esponenzialmente, richiedendo una cosiddetta "rivoluzione hardware". Nell'ultimo decennio, la miniaturizzazione ha regolato lo sviluppo delle memorie a stato solido e delle tecnologie basate sui semiconduttori. Tuttavia, il concetto innovativo di una "memoria universale" è emerso per superare il limite ultimo di riduzione delle dimensioni dei dispositivi. Infatti, questo nuovo sistema combina l'alta velocità di calcolo e l'elevata densità di archiviazione. Le memorie basate sui materiali a cambiamento di fase (PCMs) possono essere utili allo scopo, resistendo alla riduzione in scala e avendo sia una velocità di cancellazione/lettura competitiva rispetto ai sistemi di memorie primarie -come le Static/Dynamic Random Access Memory (SRAM, DRAM)- sia la grande capacità dei sistemi di archiviazione non-volatili secondari/terziari - come i Solid State Disk (SSD), gli Hard Disk Drive (HDD) e i Digital Video Disc (DVD).

L'attrattiva dei materiali a cambiamento di fase deriva dalla loro abilità di mutare velocemente e reversibilmente il loro stato da amorfo a cristallino e viceversa, attraverso impulsi ottici o elettrici. È interessante come le due fasi strutturali posseggano proprietà fisiche differenti in modo molto significativo, in particolare in termini di riflettività e conducibilità. Molti composti binari o ternari presentano queste caratteristiche, nonostante ciò le leghe di Ge-Sb-Te (GST) sono i membri di rilievo nella classe dei materiali a cambiamento di fase e sono largamente utilizzati industrialmente. Purtroppo, il maggior svantaggio è il consumo di energia relativamente alto dei PCMs, sotto forma di energia richiesta per la trasformazione di fase e di energia dissipata attraverso -primariamente- la diffusione termica.

Questa tesi segue una strategia dimensionale per i materiali GST al fine di ottimizzare la potenza richiesta nei processi di cambiamento di fase -pur mantenendo per-

formance avanzate- per una futura integrazione in innovativi dispositivi di memoria. L'approccio seguito include il caso di una struttura 2-D altamente testurizzata -chiamata super-reticolo e composta da strati alternati di GeTe e Sb_2Te_3 - e il caso di nanoparticelle 0-D di $\text{Ge}_2\text{Sb}_2\text{Te}_5$.

Il Capitolo 1 passa in rassegna lo stato-dell'arte dei materiali a cambiamento di fase, che ha stimolato le tematiche di ricerca affrontate nel presente lavoro.

La spettroscopia di assorbimento EXAFS (Extended X-Ray Absorption Spectroscopy) -brevemente presentata nella prima parte del Capitolo 2- é un potente strumento sperimentale per investigare la struttura atomica di un materiale. Nel Capitolo 3, una delle due fasi allotrope cristalline del super-reticolo (GeTe)-(Sb_2Te_3) viene descritta e rivelata nel dettaglio attraverso misure EXAFS svolte alle soglie K del germanio e dell'antimonio. Il quadro strutturale emerso viene commentato alla luce dei modelli proposti in letteratura, i quali suggeriscono un processo di cambiamento di fase nei super-reticoli che consente di risparmiare energia, ma che -sfortunatamente- é troppo semplificato.

Il Capitolo 4 affronta il problema del consumo di energia dimostrando sperimentalmente il miglioramento nel costo di energia nel processo di cambiamento di fase ottico che si verifica nelle nanoparticelle 0-D di $\text{Ge}_2\text{Sb}_2\text{Te}_5$. Qui, una transizione stabile ma reversibile dallo stato cristallino allo stato amorfo delle nanoparticelle viene indotta con un singolo impulso laser della durata di femtosecondi a bassa fluena. Considerazioni termodinamiche, ottiche e strutturali avvalorano l'evidenza sperimentale.

La sorgente laser insieme al setup utilizzato per le misure ottiche vengono descritti nella seconda parte del Capitolo 2. Il setup ottico -concepito per misurazioni risolte nel tempo- ha permesso di seguire anche i percorsi di rilassamento delle nanoparticelle foto-eccitate al di sotto della fluena critica di amorfizzazione permanente. I risultati di questo studio vengono rivelati nel Capitolo 5. Le dinamiche ultraveloci sono confrontate con simulazioni teoriche e sono modellizzate attraverso un'equazione fenomenologica. Alcune osservazioni sulle scale temporali risultanti e sui meccanismi di interazione alla base dei processi ultraveloci -mettendo in discussione la

natura del legame risonante (resonant bonding) presente nei GST- chiudono il Capitolo.

1

GENERAL INTRODUCTION

ABSTRACT

Topical technology in data storage and optoelectronic devices urges for active-materials enduring scale reduction as well as volatility, data retention and elevated read-write cycles. Here, the technological success of Ge-Sb-Te based phase-change materials -stemming from their distinctive electronic and structural peculiarities- is briefly presented. As the demand of a higher information density proceeds, nanostructures arise as potential attractive solution. An overview of the main 2-D, 1-D and 0-D examples of phase-change materials and the influence of size effects on the crucial functional parameters is introduced. Finally, the outline and the main motivations of this thesis close the chapter.

1.1 PHASE-CHANGE MATERIALS

The term phase-change materials (PCMs) can apply both to latent heat-storage and data-storage technologies. This work will refer to the class of alloys whose unique property portfolio is ideally suited for memory device applications.[1]

1.1.1 History and Functioning

In the late 1960's, Stanford R. Ovshinsky[2] proved the first fast (\sim ns) electrical transition of various type of disordered Te-based semiconductors from a low- to a high-conductive state. Interestingly, while for some stoichiometries the final state reverted back with an applied current lower than a threshold value, for low content at% of As the final state lasted, even with total current removal. He also finally foresaw the connection between the switching process and structural changes. The emerged basic concepts of (i) stability, (ii) electrical/structural contrast and (iii) reversibility related to the two allotrope solid-state phases of these semiconductors promoted Ovshinsky to be the pioneer of the field of PCMs for data storage devices. Later on, *Feinleib et al.*[3] demonstrated the same phase transformation triggered by optical pulses of different time duration and amplitude. Yet, this technology reached the commercial market in the 90s, after *Yamada et al.*[4] reported the first *fast* switching in 1987.

Fig. 1a summarizes this scenario by displaying the principle of operation of PCMs. The key aspect is the control of the optimal amount and optimal source of heat supplied. A fast and intense electrical/optical pulse allows melt-quenching (RESET) of the conductive-high reflective-*crystalline* phase. The cooling rate can reach up to 10^{10} K/s, according to the extent of the heated area and the overall thermal conductivity. The final resistive-opaque-*amorphous* phase can then recover the initial state (SET) via annealing above the crystallization (or “glass”) temperature through a longer but less intense stimulus. Accordingly, the melting ($T_{\text{melt}} \sim 900 - 950$ K) and crystallization ($T_{\text{cry}} \sim 450 - 500$ K) temperatures define the PCM functioning window. In particular, the “operating temperature” of a PCM memory lays below T_{cry} . The

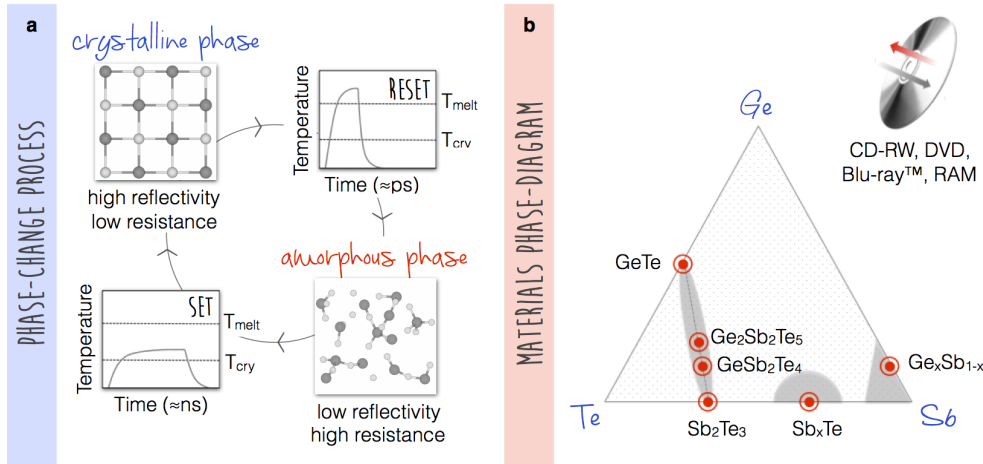


Figure 1: **a** Phase-Change material reversible switching mechanism. **b** Ternary Ge:Sb:Te phase diagram indicating the most common alloy compositions exploiting phase-change properties. Reproduced from Ref. [8].

large contrast in reflectivity the two different phases of PCMs exhibits is the core technology of the state-of-the-art optical rewritable media devices (DVDs, Blu-Ray Disc). The 1-bit logical state is encoded as a crystalline mark on an amorphous 0-bit background. Then, the information can be read by a low-power continuous diode laser, detecting the reflected light. In addition, the two-states contrast in resistivity could be exploited in the next generation of electronic solid-state memories called PRAM (Phase-Change Random Access Memory), following the current Flash memory, being non-volatile and working at speed competitive with dynamic memories (DRAM).[1; 5; 6] In this case, the state is identified by the amount of current passing through a resistor (PRAM cell). Interestingly, by combining both the optical and electronic property modulations, PCMs could be also employed in displays or data visualization applications.[7]

1.1.2 Requirements and Main Composition

Although the high-potential for several applications, PCMs must always and simultaneously fulfil a series of challenging requirements[1; 9–11]:

1. High Crystallization Temperature T_{cry} . It increases the operating temperature range and thus improves the stability and lifetime of the amorphous state within.
2. Optimal Crystallization-Rate. It should be *low* below the maximum operating temperature (~ 400 K) for longer data retention time, as well as *high* at elevated temperature (~ 850 K) leading to a fast reversal of the amorphous marks. Accordingly, the SET process optimal condition is balanced between these two opposite demands.
3. Low Melting Temperature T_{melt} . The RESET process is the most energy consuming part of the switching mechanism, setting an upper limit to the optical fluence or electric current involved in the overall process. Thus, a low T_{melt} eases the amorphization process and decreases the power consumption.
4. High Cyclability. The cell ability of switching for more than 10^6 cycles without damage ensures an extended memory durability.
5. Large Phases Contrast. Either the reflectivity or conductivity must significantly differ in the two phases, to allow an easy state identification.
6. Scalability. The data density improves as the functionality of PCMs endures scale reduction, up to nm length limit.

Over the years, materials ideally suited for memory integration -satisfying the above unique kinetics and optical/electronic prerequisites- were discovered empirically as binary or ternary compounds. Chalcogenide semiconductors (like Te, Se and S) and their alloys were chosen with respect to tetrahedral semiconductors (like Si and Ge) due to the latters' very high melting temperature and high viscosity (i.e. slow atomic diffusion) -hampering amorphization and crystallization, respectively.[12] Indeed, most PCMs are alloys located in the ternary Ge:Sb:Te-phase diagram.[5] Fig. 1b highlights the three benchmark families of phase-change chalcogenides already employed in commercial devices: (1) Sb-doped with Ge; (2) Sb_xTe -doped with Ge (for $x=2-4$); (3) GeTe- Sb_2Te_3 pseudo-binary line.[13] It is important to note that "doping" in the case of PCMs refers to some percent of concentration. Indeed, for (2) and (3) families doping with Ge is crucial for amorphous phase stabilization and for low T_{cry} in the operating temperature range. These compounds are called fast-growth materials,

i.e. μm areas develop via rapid crystallization. The members of (3) -denoted as GST- are instead nucleation-dominant materials, i.e. they produce high-density nucleation nm-sized sites. The leading and most widely employed stoichiometry of GST is the 225.[14]

1.1.3 Atomic Structure: Crystalline and Amorphous Phase

The crystal structures of the tie-line limiting cases, GeTe and Sb_2Te_3 , own peculiar features that Ge:Sb:Te materials inherit.[11] In particular, at room temperature, GeTe has a rock-salt structure, distorted along the [111]-direction forming long and short Ge-Te bonds (Peierls dimerization)[15] and with a $\sim 58^\circ$ cell angle. GeTe is made of bilayers (BL) stacked along the [0001]-direction (c-axis), as shown in Fig. 2a. The “packing” sequence is A-a-B-b-C-c where upper- and lower-case letters refer to Te and Ge species, respectively.[16–18]

Sb_2Te_3 has also a distorted rock-salt atomic arrangement[19], but the sequence becomes A-a-B-b-C-v-B-b-C-c-A-v-C-c-A-a-B, where upper- and lower-case letters refers to Te and Sb species. The excess of Te-atoms induce the formation of adjacent Te-planes connected via 2D “weak” bonds, denoted as v and named van der Waals (vdW) gaps.[16] Accordingly, Sb_2Te_3 will be referred to as made of quintuple layers (QL). See Fig. 2b for details.

As mentioned above, GST structure originates from GeTe and Sb_2Te_3 arrangements. Depending on the thermal treatment, GST crystallizes in different structures.[20] At ~ 450 K an amorphous-to-rock-salt transition occurs, defining the GST *metastable* structure. Within this NaCl-structure, the Te atoms occupy one fcc sublattice (Cl sites) while Ge, Sb and vacancies occupy randomly the other fcc sublattice (Na sites). The at% of vacancies is determined by the stoichiometry, and is proportional to $(1-x)/(3-2x)$ for $(\text{GeTe})_x(\text{Sb}_2\text{Te}_3)_{1-x}$.[21] Yet, it still presents atomic Peierls dimerization and, for GeTe-rich compositions, also a rhombohedral distortion of the unit cell.[21]

Above 650 K, the *metastable* phase converts into the *stable* packed-hexagonal struc-

ture. The vacancies arrange in layers, leading to subsequent vdW gaps formation. Several stacking sequences have been proposed in literature for this phase. The most commons are the ones proposed by: (i) *Petrov et al.* [22]: Te-Sb-Te-Ge-Te-v-Te-Ge-Te-Sb-Te; (ii) *Kooi and De Hosson*[23]: where Sb and Ge are exchanged with respect to (i); (iii) *Matsunaga et al.*[24]: with intermixing in Sb/Ge site occupation with respect to (i). It was proved[16] that intermixing is just slightly kinetically unfavourable and Te tends to maximize the number of surrounding Sb and Ge atoms (i.e. three). Hence, it is accepted that the *stable* phase is characterized by Sb/Ge mixing with Sb-rich planes located towards the vdW gaps.[25] Fig. 2c sketches both the metastable and stable structure of the representative alloy GST 225. The “double” or “triple” coloured balls identify the mixing of Ge and Sb or of Ge, Sb and vacancies, respectively. Ge-rich planes are off from the vdW gaps.

The atomic structure of the *amorphous* phase is not unique, since it strictly depends on growth conditions and on thermal history. As a general result, from both theoretical calculations and experimental measurements, there is evidence of homopolar Ge-Ge and Ge-Sb bonds predominance with respect to homopolar Te-Te and Sb-Sb bonds. In addition, the coordination numbers rather deviate from the so-called *8-N* rule, for which the amount of first neighbours in a covalent environment is given by 8 minus the number of valence electrons of an atom. In particular, Ge not only is found in a 4-fold (tetrahedral) coordination -as expected by the *8-N* rule- but preferentially in a 6-fold (octahedral) coordination.[11]

1.2 GE-SB-TE NANOSTRUCTURES

The roadmap towards the ultimate Moore’s law limit[26], in the case of phase-change memory technology must take in consideration the scaling properties of both the constituent phase-change material and the overall phase-change device. 2-D (thin films[20; 27]), 1-D (nanowires[28; 29]) and 0-D (nanoparticles[30–33]) GST alloys have been successfully produced and studied. Accordingly, it was shown that size

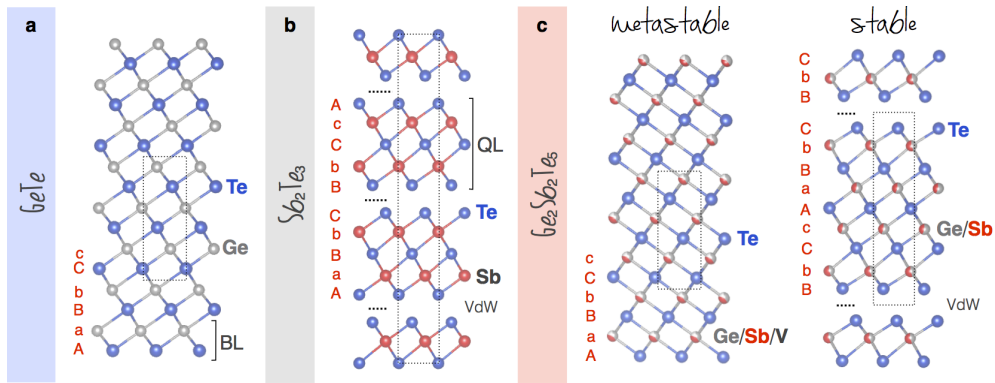


Figure 2: Structural models and unit cells (dotted lines) for: **a** GeTe; **b** Sb₂Te₃; **c** metastable and stable GST 225. Grey, red and blue spheres denote Ge, Sb and Te atoms, respectively. In GST model, the spheres are colored according to the fractional occupation of elements and vacancies. The stacking sequences are indicated in red on the left side of the models. (V = vacancy, VdW = van der Waals gap, BL = bilayer, QL = quintuple layer, V = vacancy)

(i.e. μm , nm) and spatial confinement (i.e. 2-D, 1-D, 0-D) can strongly affect the physical properties of PCMs with respect to the single crystal analogues.

1.2.1 2-D: Thin Films and Superlattice Structures

Deposition of thin films (from 10 nm down to 1 nm) via Molecular Beam Epitaxy (MBE) or Physical Vapour Deposition (PVD) allows for an accurate thickness and flatness control. In the film size-range below 20 nm, T_{melt} markedly decreases -with respect to the nominal bulk value- while, correspondingly, T_{cry} increases.[14; 20] These trends reduce the amorphization energy request and improve data retention -hindering accidental crystallization, respectively. Yet, an ultimate scaling limit is defined when T_{cry} and T_{melt} coincide, preventing the switching process to occur. For instance, the thinnest GST film which could be crystallized is 2 nm thick.[20]

Also thermal conductivity revealed a scaling behaviour, decreasing linearly with dimension.[34] The dissipation of thermal power is thus limited, suggesting a favourable advantage in scale reduction.

For thin film of GST (20 nm), Kolobov and coworkers[35] proposed a new low-energy order-disorder transition. The switching mechanism is based on the so-called “umbrella-flip” model. It reports that, on ultrashort time-scales, non-thermal structural rearrangements can take place upon crystallization. In particular, Ge atoms change coordination from tetrahedral to octahedral. Yet, although being an appealing simple model, it is unlikely to be the common phase-change mechanism, due both to the low concentration of tetrahedral Ge-sites in the amorphous initial phase and to the weakness of the resulting final state.[9; 36; 37]

Hence, a lot of interest and effort is currently devoted to uncover the complex physical origin of the high contrast between the two phases,[37–39] as well as of the atomistic representation of the switching mechanism.[40–42]

Within this framework, highly-textured thin films were developed. It is the case of “superlattice-like” chalcogenides, where nano-scale GeTe and Sb₂Te₃ units are alternatively deposited at room temperature.[43–46] They combined the thermal stability of the former and the fast-switching of the latter. Fig. 3a shows an high resolution TEM image of a GST chalcogenide superlattice (courtesy of J. Momand, also in Ref. [47]). Chalcogenide superlattice will be topic of Chapter 3.

1.2.2 1-D: Nanowires

Chalcogenide nanowires (NWs)[48] were synthesized using the metal catalyst-mediated vapour–liquid–solid (VLS) process.[29; 49] In the case of 40–80 nm diameter GeTe nanowires[29], it was found that: (i) the crystal structure was fcc; (ii) T_{melt} presents a 46% reduction with respect to the bulk value; (iii) a native GeO₂ outer capping layer prevents oxidation and evaporation of the inner GeTe, improving device fabrication and performances. Accordingly, Ge₂Sb₂Te₅ NWs -applied in real switching devices- showed substantial size effects, in terms of re-crystallization time and activation energy.[49] Fig. 3b shows a TEM image of representative GST nanowires of ~ 200 nm diameter. [50]

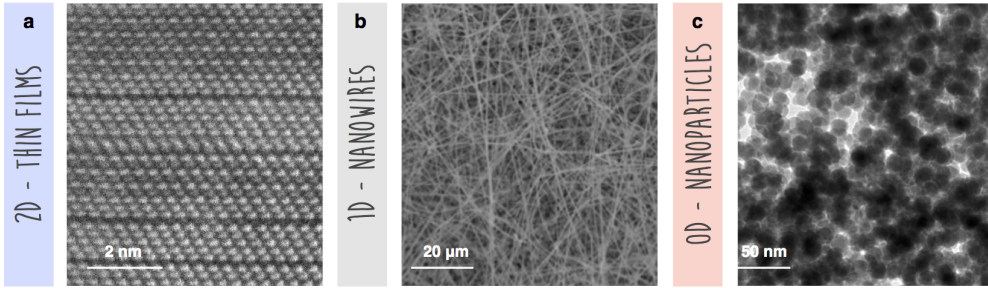


Figure 3: High-resolution TEM examples images of: **a** GST-superlattice thin film (courtesy of J. Momand); **b** GST nanowires (adapted from Ref. [50]); **c** GST nanoparticles (courtesy of B. Chen, also in Ref. [33]).

1.2.3 0-D: Nanoparticles

Various growth techniques were used in order to produce chalcogenide nanoparticles (NPs). Despite being the easiest fabrication method, laser ablation led to a broad NPs size-distribution, from few to tens of nanometers in diameter.[31; 32; 51] Alas, there is no common agreement on the transitional temperatures (amorphous-fcc, fcc-hexagonal) and final atomic structures.[31; 32; 51] Electron beam lithography set a 20 nm limit to the minimum NPs size, and produced amorphous as fabricated NPs that after heating became polycrystalline -with 10 nm crystal size.[52] To overcome this limit, self-assembly[53] or solution-chemistry[54] approaches were used. In particular, the GeTe nanoparticles case of study is of uttermost importance since a drop in the T_{melt} was observed with reducing particles diameter and the minimum diameter -for the switching process to occur- resulted to be less than 2 nm.[54] Fig. 3c shows a high resolution TEM image of GST nanoparticles of ~ 10 nm diameter (courtesy of B. Chen, also in Ref. [33]). GST nanoparticles will be topic of Chapter 4 and Chapter 5.

1.3 THESIS MOTIVATION AND OUTLINE

The target of this thesis is to address the following questions:

Research Question 1. *Do “superlattice-like” GST materials represent a real challenging scenario with improved switching properties for future device technology?*

Research Question 2. *Does optical switching occur in 0-D GST materials? How do 0-D GST materials represent a valid alternative to higher-dimension counterparts in terms of energetics?*

Hence, Chapter 3 reports an atomistic insight on the atomic structure of highly-textured crystalline GeTe-Sb₂Te₃ superlattices, with very thin sublayers. Accordingly, the principal features of the experimental method used -i.e. Extended X-Ray Absorption Spectroscopy (EXAFS)- are discussed in details (first part of Chapter 2). The goal is to define the initial state structure for testing the feasibility of a recently proposed low-energy switching process, thus addressing Research Question 1.

Chapter 4 and Chapter 5 investigate the optical properties of crystalline Ge₂Sb₂Te₅ NPs of 7 – 10 nm size. The experimental setup and the related laser pulse features are carefully described (second part of Chapter 2). It is proved that an ultrafast single pulse -with very low fluence- can laser amorphize < 10 nm size particles. This observation is supported by a series of complementary measurements (optical microscope, XRD, optical transmission, absorption spectroscopy). In addition, complete time-resolved spectra -without inducing any phase-change- are presented and commented. The aim is to observe the electronic dynamics occurring in 0-D systems and to highlight differences or similarities with higher-dimension phase-change materials. Therefore, the work described here is an attempt to answer Research Question 2.

BIBLIOGRAPHY

- [1] M. Wuttig and N. Yamada. *Nature Materials*, 6(11):824–832, 2007.
- [2] S. R. Ovshinsky. *Physical Review Letters*, 21:1450–1453, 1968.
- [3] J. Feinleib, J. deNeufville, S. C. Moss, and S. R. Ovshinsky. *Applied Physics Letters*, 18(6):254–257, 1971.
- [4] N. Yamada, E. Ohno, N. Akahira, et al. *Japanese Journal of Applied Physics*, 26: 61–66, 1987.
- [5] S. Raoux, W. Wełnic, and D. Ielmini. *Chemical Reviews*, 110(1):240–267, 2010.
- [6] G. W. Burr, M. J. Breitwisch, M. Franceschini, et al. *Journal of Vacuum Science & Technology B*, 28(2):223–262, 2010.
- [7] P. Hosseini, C. D. Wright, and H. Bhaskaran. *Nature*, 511(7508):206–211, 2014.
- [8] V. L. Deringer, R. Dronskowski, and M. Wuttig. *Advanced Functional Materials*, 25(40):6343–6359, 2015.
- [9] K. Shportko, S. Kremers, M. Woda, et al. *Nature Materials*, 7(8):653–658, 2008.
- [10] M. H. R. Lankhorst, B. W. S. M. M. Ketelaars, and R. A. M. Wolters. *Nature Materials*, 4(4):347–352, 2005.
- [11] A. D. A. Lencer. *Design rules, local structure and lattice dynamics of phase change materials for data storage applications*. PhD thesis, RWTH Aachen University, 2010. URL <http://publications.rwth-aachen.de/record/63829>.
- [12] S. Raoux and M. Wuttig. *Phase Change Materials*. Springer US, 2008.
- [13] J. Oosthoek. *Structural and electrical characterization of phase change memory line cells*. PhD thesis, University of Groningen, 2014.
- [14] R. E. Simpson, M. Krbal, P. Fons, et al. *Nano Letters*, 10(2):414–419, 2010. PMID: 20041706.
- [15] J. Gaspard. *Comptes Rendus Physique*, 17:389–405, 2016.
- [16] J. L. F. Da Silva, A. Walsh, and H. Lee. *Physical Review B*, 78:224111, 2008.
- [17] T. Nonaka, G. Ohbayashi, Y. Toriumi, Y. Mori, and H. Hashimoto. *Thin Solid Films*, 370(1-2):258–261, 2000.
- [18] P. A. Vermeulen, A. Kumar, G. H. ten Brink, G. R. Blake, and B. J. Kooi. *Crystal Growth & Design*, 16(10):5915–5922, 2016.

- [19] K. Kifune, Y. Kubota, T. Matsunaga, and N. Yamada. *Acta Crystallographica Section B*, 61(5):492–497, 2005.
- [20] S. Raoux, J. L. Jordan-Sweet, and A. J. Kellock. *Journal of Applied Physics*, 103(11):114310, 2008.
- [21] T. Matsunaga, H. Morita, R. Kojima, et al. *Journal of Applied Physics*, 103(9):093511, 2008.
- [22] I. Petrov, R. Imamov, and Z. Pinsker. *Sov. Phys. Cryst.*, 13:339, 1968. cited By 2.
- [23] B. J. Kooi and J. T. M. De Hosson. *Journal of Applied Physics*, 92(7):3584–3590, 2002.
- [24] T. Matsunaga, N. Yamada, and Y. Kubota. *Acta Crystallographica Section B*, 60(6):685–691, 2004.
- [25] J. Momand. *Structure and Reconfiguration of Epitaxial GeTe/Sb₂Te₃ superlattices*. PhD thesis, University of Groningen, 2017.
- [26] G. E. Moore. *Proceedings of the IEEE*, 86(1):82–85, 1998.
- [27] H. Satoh, K. Sugawara, and K. Tanaka. *Journal of Applied Physics*, 99(2):024306, 2006.
- [28] Y. Jung, S.-H. Lee, D.-K. Ko, and R. Agarwal. *Journal of the American Chemical Society*, 128(43):14026–14027, 2006. PMID: 17061875.
- [29] X. Sun, B. Yu, G. Ng, and M. Meyyappan. *The Journal of Physical Chemistry C*, 111(6):2421–2425, 2007.
- [30] H. Yoon, W. Jo, E. Lee, et al. *Journal of Non-Crystalline Solids*, 351(43):3430 – 3434, 2005.
- [31] D.-S. Suh, E. Lee, K. H. P. Kim, et al. *Applied Physics Letters*, 90(2):023101, 2007.
- [32] H. S. Choi, K. S. Seol, K. Takeuchi, J. Fujita, and Y. Ohki. *Japanese Journal of Applied Physics*, 44(10R):7720, 2005.
- [33] B. Chen, G. H. ten Brink, G. Palasantzas, and B. J. Kooi. *Scientific Reports*, 6:39546, 2016.
- [34] J. P. Reifenberg, M. A. Panzer, S. Kim, et al. *Applied Physics Letters*, 91(11):111904, 2007.
- [35] A. V. Kolobov, P. Fons, A. I. Frenkel, et al. *Nature Materials*, 3(10):703–708, 2004.
- [36] C. Lang, S. A. Song, D. N. Manh, and D. J. H. Cockayne. *Physical Review B*, 76:054101, 2007.
- [37] B. Huang and J. Robertson. *Physical Review B*, 81:081204, 2010.

- [38] J. Akola and R. O. Jones. *Physical Review B*, 76:235201, 2007.
- [39] T. Siegrist, P. Jost, H. Volker, et al. *Nature Materials*, 10(3):202–208, 2011.
- [40] B.-S. Lee, G. W. Burr, R. M. Shelby, et al. *Science*, 326(5955):980–984, 2009.
- [41] A. V. Kolobov, M. Krbal, P. Fons, J. Tominaga, and T. Uruga. *Nature Chemistry*, 3(4):311–316, 2011.
- [42] W. Zhang, A. Thiess, P. Zalden, et al. *Nature Materials*, 11(11):952–956, 2012.
- [43] T. C. Chong, L. P. Shi, R. Zhao, et al. *Applied Physics Letters*, 88(12):122114, 2006.
- [44] T. C. Chong, L. P. Shi, X. Q. Wei, et al. *Physical Review Letters*, 100:136101, 2008.
- [45] C. Chia Tan, L. Shi, R. Zhao, et al. *Applied Physics Letters*, 103(13):133507, 2013.
- [46] P. Long, H. Tong, and X. Miao. *Appl. Phys. Expr.*, 5(3):031201, 2012.
- [47] J. Momand, R. Wang, J. E. Boschker, et al. *Nanoscale*, 7:19136–19143, 2015.
- [48] L. Lazzarini and E. Rotunno. *Materials Science in Semiconductor Processing*, 65:77 – 87, 2017.
- [49] S.-H. Lee, Y. Jung, and R. Agarwal. *Nature Nanotechnology*, 2(10):626–630, 2007.
- [50] P. Nukala. Crystal-amorphous transformation via defect-templating in phase-change materials, 2015. URL https://www.researchgate.net/publication/304047426_Crystal-Amorphous_Transformation_Via_Defect-Templating_In_Phase-Change_Materials.
- [51] G.-S. Park, J.-H. Kwon, M. Kim, et al. *Journal of Applied Physics*, 102(1):013524, 2007.
- [52] S. Raoux, C. T. Rettner, J. L. Jordan-Sweet, et al. *Journal of Applied Physics*, 102(9):094305, 2007.
- [53] Y. Zhang, H.-S. P. Wong, S. Raoux, et al. *Applied Physics Letters*, 91(1):013104, 2007.
- [54] M. A. Caldwell, S. Raoux, R. Y. Wang, H.-S. Philip Wong, and D. J. Milliron. *J. Mater. Chem.*, 20:1285–1291, 2010.

2

EXPERIMENTAL METHODS

ABSTRACT

X-Ray Absorption Fine-Structure (XAFS) spectroscopies yield detailed information about the physical, chemical and structural environment of a selected-element atom. Although the need of X-rays (between 500 eV up to 500 keV) -and thus of tunable synchrotron radiation- makes them less accessible than other laboratory techniques, their power relies on their ability to span over all periodic-table elements, ordered and disordered systems, dilute and dense concentrations, and up to μm -size samples, without destroying the probed material.[1] A vast literature of books and reviews about XAFS is currently available, covering theoretical, experimental and data-analysis aspects in several disciplines (see Ref. [1; 2] and therein). Hence, the first part of this chapter will provide just an essential overview of the XAFS fundamentals relevant to our measurements context, presented in Chapter 3.

Ultrafast laser systems producing ultrashort (~ 100 fs) light pulses allow to investigate the dynamics of phenomena occurring up to femtoseconds timescales. The second part of this Chapter briefly describes the laser source and the setup used for the ultrafast optical static and time-resolved measurements shown in Chapter 4 and Chapter 5.

2.1 X-RAY ABSORPTION FINE STRUCTURE

2.1.1 Basic Principles

The *photoelectric effect* lies at the base of the X-Ray absorption process. An X-Ray with energy E is absorbed by a core-level electron with binding energy E_0 when $E > E_0$. The excess of energy is given to a photoelectron, propagating as a spherical wave in the continuum with *wavenumber*:

$$k = \frac{2\pi}{\lambda} = \sqrt{\frac{2m(E - E_0)}{\hbar^2}} \quad (1)$$

where m is the electron mass and \hbar is the Planck's constant. For absorption to occur, the quantum states in the conduction band must be at the same time *available* (i.e. unoccupied) and *suitable* (i.e. have the right energy and selection rules) for the excited photoelectron. The process probability is quantified by the absorption coefficient μ . As E increases, the absorption probability has a sharp rise (i.e. an edge jump) approaching E_0 and the photoelectron travels with decreasing wavelength $\lambda \sim \sqrt{1/(E - E_0)}$. In condensed matter, a part of the photoelectron wavefunction can be scattered-back from the neighbours of the absorbing atom, selected by choosing a specific core-level energy E_0 . Hence, at the absorber location, the presence of the back-scattered photoelectron modifies the availability of unfilled states. Accordingly, the process probability μ is modulated, oscillating around the absorption coefficient of an isolated atom μ_0 . Fig. 4 illustrates a cartoon of the whole mechanism. In particular, it is possible to note that constructive (S_0, S_1) or destructive (S_2) interference can occur between the outgoing and the back-scattered photoelectron, giving rise to oscillations in μ . In addition, the spectrum region within ~ 30 eV from E_0 is called NEXAFS (Near Edge XAFS) while the one up to few keV above the edge is called EXAFS (Extended XAFS). Despite the fundamental physical description of both regimes being identical, this thesis will mainly focus on EXAFS.

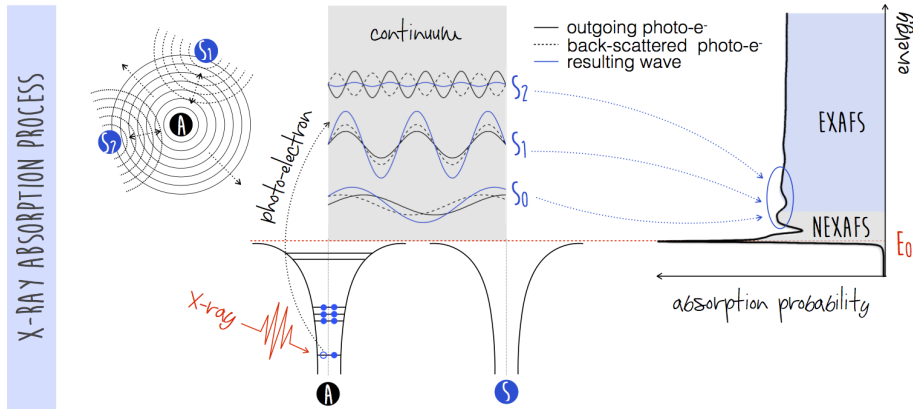


Figure 4: Schematic representation of the X-ray Absorption spectroscopy. The excited photoelectron can be considered as an outgoing spherical wave that can interfere constructively or destructively with the backscattering waves coming from the neighbouring atoms. The oscillations recorded in the extended energy region above the absorption edge, reflect the effects of interference. Reproduced from Ref. [1].

Formally, X-Ray absorption is a quantum transition from an *initial* state $\langle i |$ (X-Ray and core electron) to a *final* state $| f \rangle$ (core hole and photoelectron). The transition probability can be described by the Fermi's Golden Rule:

$$\mu(E) \propto |\langle i | H | f \rangle|^2 \quad (2)$$

with H the interaction hamiltonian and $| f \rangle = | f_0 + \Delta f \rangle$ the actual final state since the photoelectron wavefunction is modified by the scattering from the neighbouring atoms. By properly expanding Eq. 2 one obtains:

$$\mu(E) \propto \mu_0(E) [1 + \chi(E)] \quad (3)$$

where $\mu_0(E) = |\langle i | H | f_0 \rangle|^2$ is the isolated atom absorption (smooth background function) and $\chi(E) \propto \langle i | H | \Delta f \rangle$ accounts for the EXAFS fine structure, ascribing the origin of oscillations to the interaction between the scattered part of the photoelectron and the absorber. Inserting both the interaction term quantized form ($\rho \cdot A$, with ρ momen-

tum and A vector potential) and the photoelectron wavefunction spherical form (e^{ikr}/kr) in the $\chi(E)$ integral, and converting E in k , the EXAFS final equation is given by:

$$\chi(k) = \sum_j S_0^2 N_j F_j(k) e^{-2k^2 \sigma_j^2} \left[\frac{e^{-2R_j/\lambda_j(k)} \sin [2kR_j + \delta_j(k)]}{kR_j^2} \right] \quad (4)$$

In the following, each term will be presented and explained.

The sum is over each *coordination shell* j , a group of identical type of neighbouring atoms at the same distance from the absorber. It is important to note that shells of similar Z (atomic number) and sufficiently near ($< 0.05\text{\AA}$) cannot be easily distinguished.

S_0^2 is the *amplitude reduction factor*, accounting for the relaxation of the remaining $Z - 1$ electrons in the absorber due to the formation of the core-hole. This term is k -independent, thus is a constant with value in the range between 0.6 and 1.0.

N is the number of atoms in the same *coordination shell*. N and S_0^2 are completely correlated with each other.

$F_j(k)$ is the backscattering amplitude, different for distinct type of scatterers.

The distance R_j between the absorber and the scatterers of a particular shell can slightly vary due to thermal excitations and structural disorder. Thus, the contributions of all scatterers can be de-phased and is included through the factor $e^{-2k^2 \sigma_j^2}$, where σ_j^2 is usually referred as Debye-Waller factor and is the mean square displacement of the backscatter j and the absorber.

The last term in parentheses represents the damped spherical real photoelectron wavefunction. The first exponential accounts for the possible *inelastic scattering* events. The photoelectron scatters from different sources losing energy, and comes back to the absorber. The maximum distance it can travel before the core-hole recombination is the *inelastic mean-free path* $\lambda_j(k)$. The $\sin [2kR_j + \delta_j(k)] / [kR_j^2]$ part is the real spherical wave where $\delta_j(k)$ is the overall phase-shift ascribed to the interaction of the photoelectron with the varying potential of the absorber and backscattered atom.

Usually, the photoelectron can scatter from more than just a single nearby atom. This will produce a series of multiple scattering paths which contributes significantly

to the EXAFS oscillations, in particular at distances beyond the first (nearest) coordination shell. The equation above is still valid, with few adaptations. In particular, j will be a scattering path, $F_j(k)$ and $\delta_j(k)$ will be *effective* scattering amplitude and phase-shift, considering each atom in the scattering path. N_j accounts for the degeneracy of the scattering path j . This *path-formalism* is powerful since single and multiple scattering paths can be treated equally.

2.1.2 Data Collection and Reduction

There are two possible approaches for collecting XAFS data: (i) *transmission* mode and (ii) *emission* mode. The first method follows the Beer-Lambert Law and the absorption coefficient is given by:

$$\mu(E) = \frac{1}{d} \ln \left(\frac{I_0}{I_t} \right) \quad (5)$$

where d is the sample thickness, I_0 and I_t are the X-Ray intensity *before* and *after* the interaction with the sample.

In the second mode, either photoelectrons or X-Ray photons can be detected, due to two different mechanisms of decay occurring simultaneously but with different probabilities. In the Auger effect, an electron from higher energy levels fills the core-hole produced by X-Ray absorption and releases its energy to a second electron that is emitted in the continuum (or even ejected). A cascade of secondary emissions occurs until complete atom relaxation. This mechanism dominates in the Soft X-Ray regime and for light elements (low Z). Alternatively in fluorescence, the energy from de-excitation is given to X-Ray photons of defined energies. These energies are called “emission lines” and are typical of each element. For instance, K_β is the fluorescence line originated from an M-shell electron drop. This mechanism dominates instead in the Hard X-Ray regime and for heavy elements (high Z).

The absorption coefficient measured in fluorescence mode -minimizing the *self-absorption* effects (thin, thick and dilute, or grazing emission)- is given by:

$$\mu(E) \propto \frac{I_f}{I_0} \quad (6)$$

Therefore, an initial and a fluorescence/transmitted intensity signals are measured. A data reduction is needed in order to extract the fine structure $\chi(k)$. There are few main steps to be followed:

1. *Conversion*: from collected intensities as a function of X-Ray energy to absorption coefficient $\mu(E)$ at a specific element absorption edge;
2. *Energy Calibration*: the $\mu_r(E)$ of a reference material (calibration foil) is collected simultaneously and its $E_{0,r}$ -defined as the derivative first maximum- is shifted according to the tabulated value. The position of the sample E_0 is equivalently shifted.
3. *Normalization*: the pre-edge and post-edge regions are fitted with a line and a polynomial, respectively. These fits are subtracted from the experimental data. $\mu(E)$ is divided by the edge step $\Delta\mu$, so that the spectrum is *normalized* going from 0 below the edge to 1 above the edge.
4. *Background Subtraction*: starting from Eq. 3, the isolated XAFS is usually written as $\chi(E) = [\mu(E) - \mu_0(E)]/\Delta\mu$. After normalization, $\Delta\mu = 1$ and $\mu_0(E)$ -the background function- is fitted involving connected splines (1st, 2nd or 3rd order polynomials).
5. *Extraction*: of the fine structure χ from μ and convert the dependence from the energy E to the wavevector k ;
6. *Fourier Transform*: the fine structure signal $\chi(k)$ is weighted by k , k^2 or k^3 to compensate for the damped oscillations at high k -values. In addition, a window-function is used to eliminate noise due to sharp truncation of experimental data. The Fast Fourier Transform can thus be performed producing a complex wave $\chi(R)$ in radial space. The FFT magnitude is not simply a radial distribution

function, due to the contribution of both scattering factor $F(k)$ and phase-shift $\delta(k)$.

The program ATHENA[2] can entirely complete the above XAS data-processing.

2.1.3 Data Analysis

The program ARTEMIS[2] performs a least-square refinement analysis of the EXAFS data, relying on theoretical structural models of the investigated materials. As already mentioned, in *path-formalism* EXAFS contains information on the length R_j , degeneracy N_j and Gaussian variation σ_j^2 of the j -th scattering path produced by the outgoing photoelectron from the absorber. All the possible scattering paths j -below a user-defined length cut-off- are calculated using FEFF algorithm, based on an ab-initio self-consistent method. Each path stores the effective backscattering amplitude $F_{eff,j}(k)$, the phase shift $\delta_j(k)$ and the mean free path of electrons $\lambda_j(k)$. Therefore, according to Eq. 4, the fitting procedure will involve more and more independent parameters ($N_j S_0^2$, ΔR_j , σ_j) as long as the number of path increases. Nonetheless, the final number is limited by the data range Δk and ΔR , according to the Nyquist theorem: $N_p = [(2\Delta k \Delta R)/\pi + 2]$. Finally, the R-factor accounts for the fit goodness. Typically, values below 0.05 are acceptable.

2.2 ULTRAFAST EXPERIMENTAL APPARATUS

2.2.1 The Laser Source

Fig. 5 sketches a schematic diagram of the optical source available at the T-ReX laboratory (Elettra Synchrotron, Trieste). The core of such system is the oscillator (Coherent® Mira), where an active medium (Ti:Sapphire crystal, i.e. Titanium doped Al_2O_3) is placed inside the resonator cavity. The oscillator is pumped by a continuous laser (Coherent® Verdi-5) generating radiation with central wavelength of 532 nm and with 5 W average power. Ti:Sapphire has a non-linear index of refraction -depending

on the strength of the incoming radiation, and a large gain bandwidth. The optical Kerr effect -occurring inside this active rod- leads simultaneously to a self-focusing (lensing) process and a self-phase modulation: the whole mechanism is called “Self-Mode Locking”.[3] When radiation travels along the cavity axis, the gain medium amplifies a specific wavelength range via spontaneous and stimulated emission and a series of longitudinal modes builds up with a frequency separation of $c/2L$ -where c is the speed of light and L is the cavity optical length. Yet, both phase and amplitude of these modes is random. Only when the phase ϕ is “self-locked”, constructive and destructive interference can occur at the same instant $T_0 = (\phi/2\pi)T$ -with $T = 2L/c$ the round trip period, also called the oscillator *repetition rate* (r.r.) -also defined as the number of pulses per unit of time. Thus, the oscillator output is characterized by successive pulses centered at $T_0 + nT$, with n integer, supporting the several allowed longitudinal modes.[3; 4] In particular, our oscillator has a repetition rate of 76 MHz and the mode-locking generates near-IR pulses with a bandwidth of ~ 50 nm centered at 800 nm. The temporal duration of each pulse $\Delta t \sim 40$ fs is roughly equal to the inverse of the bandwidth $\Delta\nu = 25$ THz spanned by the modes. The average power is ~ 0.35 W, corresponding to an energy per pulse of 4.5 nJ. Each outgoing pulse is then sent to the Legend Amplifier system, undergoing: (i) a time-stretching up to ps, to avoid damage of the following active medium; (ii) an intensity amplification via interaction with the gain medium (Ti:Sapphire), pumped by a pulsed visible laser (Coherent® Evolution) with r.r. 1 kHz; (iii) time-compression down to the 100 fs regime.[5] Therefore, the final output from this complex laser system consists of fundamental pulses with 800 nm wavelength (1.55 eV), with a temporal duration of ~ 80 fs, a repetition rate of 1 kHz and an energy per pulse of about 1.5 mJ. The r.r. of the laser source can be decreased up to single-shot events.

2.2.2 The Optical Setup

Once intensity-amplified and time-compressed, the laser pulses are delivered to the optical setup optimized for fluence-dependent, static and time-resolved transmittivity measurements. Fig. 6 displays the layout of the experimental setup. Upon incidence onto a polarizing beamsplitter, the fundamental (800 nm) s-polarized light

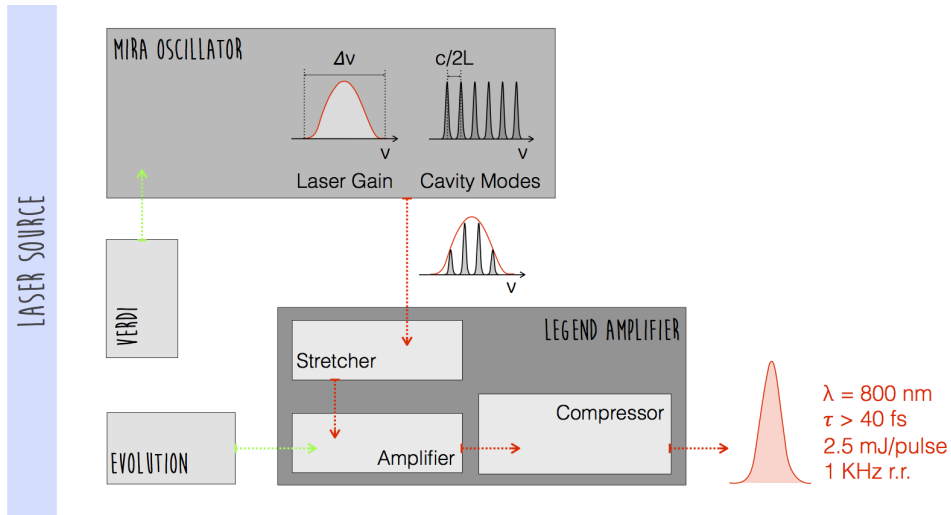


Figure 5: Sketch of the laser source available at T-ReX laboratory (Elettra Synchrotron-Trieste). The Verdi laser pumps the Mira Oscillator. The outgoing pulses then pass through the Legend Amplifier system, pumped by the pulsed Evolution laser, where they increase their energy and are compressed in time. Adapted from Ref. [5]

is reflected while the p-polarized light is transmitted. Therefore, the incoming laser beam is separated and travels along two different optical paths. The reflected beam is called “probe”, since it explores a specific property of the sample under study. It goes through a combination of polarizer(V)-half wave plate-polarizer(H) in order to adjust the pulse intensity. Then, a first plano-convex lens focuses the beam onto the sample and a second plano-convex lens re-collimates the transmitted light collected by a photodiode. This is the conventional configuration for “static” transmittivity measurements. Yet, when other pulses excites the sample *before, in coincidence or after* the arrive of the probe pulses, this configuration is defined “time-resolved”. In brief, the probe explores the evolution in time of the out-of-equilibrium sample transmittivity. Accordingly, we made use of the polarizing beamsplitter transmitted beam as the “pump”. A back-reflector mounted on a mechanical delay-stage modifies the relative optical path length between the pump and the probe pulses. Light is focused on a BBO non-linear crystal (type I), leading to Second Harmonic (SH) Generation with pulses at 400 nm. Also here, the beam goes through a combination of polarizer(H)-half wave plate-polarizer(V) in order to adjust the pulse intensity, up to extremely low values. A chopper reduces the pump pulses frequency from 1 kHz to 500 Hz,

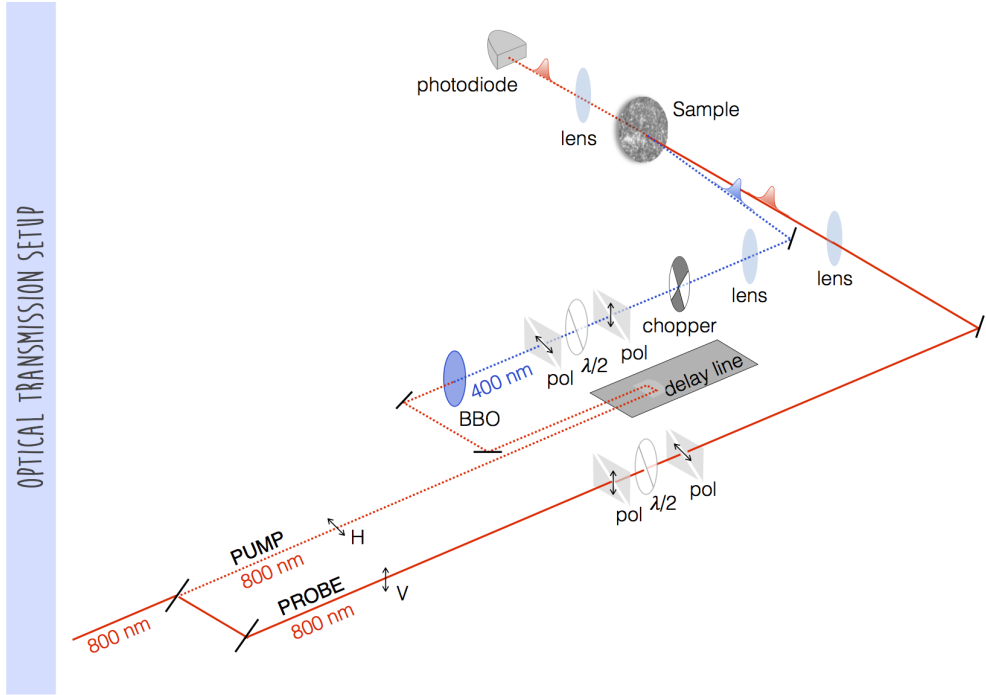


Figure 6: Sketch of the optical setup.

yielding stroboscopic measurements with low signal-to-noise. Finally, a plano-convex lens focuses the beam on the sample -at normal incidence- in spatial overlap with the probe beam. The beam profile is of Gaussian-shape. Knife-edge measurements determined the pump and probe spot-sizes (w_x , w_y), defined as the $1/e^2$ intensity level. In particular, the 400 nm pump spot is elliptic with $w_x = 88(2) \mu\text{m}$ and $w_y = 68(2) \mu\text{m}$, while the 800 nm probe spot is smaller with $w_x = 26(1) \mu\text{m}$ and $w_y = 23(1) \mu\text{m}$, to ensure transmittivity measurements on an uniformly excited sample area. Therefore, the average fluence F_{avg} (mJ/cm^2) is defined as the laser pulse energy divided by the $1/e^2$ area of the spot.

BIBLIOGRAPHY

- [1] M. Newville. *Reviews in Mineralogy and Geochemistry*, 78(1):33, 2014.
- [2] B. Ravel and M. Newville. *Journal of Synchrotron Radiation*, 12(4):537–541, 2005.
- [3] J.-C. Diels and W. Rudolph. *Ultrashort Laser Pulse Phenomena*. Academic Press, 2006.
- [4] B. Casarin. *Scattering mechanisms in the optically excited electronic states of two topologically protected systems Sb₂Te₃ and Sb₂Te*. PhD thesis, Università degli studi di Trieste, 2014.
- [5] A. Simoncig. *The role of the electron recoiling mechanism in coherent light high-order harmonics generation: from the source to the applications*. PhD thesis, Università degli studi di Trieste, 2010.

3

LOCAL STRUCTURE OF GST SUPERLATTICES

ABSTRACT¹

A superlattice is defined as a periodic structure of nm-thick alternating layers of at least two different materials. This highly-ordered structure has been demonstrated to dramatically improve the optical and electrical performances of the chalcogenide based phase-change materials. They are shown to operate with lower power threshold and faster switching time with respect to their bulk counterparts.[1–4] This performance breakthrough has been ascribed to the particular stacking layout of chalcogenide superlattices, resulting in a thermal transport reduction and thus enabling a higher temperature raise for the same absorbed power. In this perspective, unravelling the atomistic structure that originates the improvements is paramount in order to design nanoscale structures with even enhanced functional properties.

The following study falls in this context by assessing the in-depth atomistic details of the as-grown highly-textured epitaxial [GeTe (1 nm) / Sb₂Te₃ (3 nm)] superlattice - herein named chalcogenide superlattice (CSL) - which is grown fully crystalline at high temperature.

In this Chapter, the Ge and Sb local atomic environment at the interface between the GeTe and Sb₂Te₃ layers is reported. Supported by high-resolution TEM and an extended Morlet Wavelet-Transform analysis, a local and non-destructive technique like EXAFS reveals that there is not a sharp boundary between the alternate layers forming the superlattice structure. In particular, we will show that the GeTe bilayers (BLs) are not isolated but intercalated within 1 Sb₂Te₃ quintuple layer (QL), where the external Sb layers are intermixed with Ge atoms.

This result -opposing to previous atomic structure models proposed in literature- gives also a new perspective for the CSLs switching process.

¹This chapter has originally been published as Casarin B. et al., *Revisiting the Local Structure in Ge-Sb-Te based Chalcogenide Superlattices*, Scientific Reports, 6, 22353, (2016).

3.1 RECENT ADVANCES

The search of a compromise between a high-crystallization speed and a high-stability lies at the base of the performance optimization of PCMs-based non-volatile memory devices. Superlattice-like structures -obtained via alternating deposition of two different phase-change materials- were proposed as a possible solution. In particular, the choice of GeTe and Sb_2Te_3 takes advantage of the high stability of the former and the fast crystallization speed of the latter.[1]

Recently, by increasing the superlattice deposition temperature (~ 550 K) and by reducing the GeTe sublayer thickness (down to 1 nm), interfacial PCMs (iPCMs) were designed.[5] The improvements obtained for this particular structure are explained by a refined atomic switching process model, circumventing pure mass melting.[6–10] The underlying idea is that in 1 nm only two GeTe bilayers (BLs) are present and are the active ones. As a consequence, a change in the local Ge atomic bonding occurs and confines the motion in one dimension. The two reversible phases of iPCMs are thus claimed to be both crystalline. Correspondingly a reduction of the entropy variation with respect to a classic order-disorder transition is expected. Nonetheless, a nominal 1 nm of GeTe corresponds closely to 3 BLs[11], therefore querying the actual feasibility of the described Ge bonding exchange. Hence, since the GeTe sublayer plays a crucial role in defining the fundamental phase-change microscopic properties, establishing the GeTe atomistic nature as well as its interface with Sb_2Te_3 is a mandatory and pivotal point.

Most of structural reports on these chalcogenide superlattices are based upon Transmission Electron Microscopy (TEM) and (non-resonant) X-ray diffraction studies. X-ray diffraction probes the two-body correlation function over tens of nanometers.[12] Yet, the atomic arrangement can only be derived from a comparison of model simulations with the measured data, which presents significant challenges for an unambiguous identification of the atomic arrangement. Conversely, TEM is capable of providing high-resolution structural information but is characterized by a limited atomic contrast and resolution (up to 1 Å). These shortcomings create a need for complementary techniques such as EXAFS. Due to the correlation between the absorber and the

backscatter through the emitted photoelectrons excited by X-rays, EXAFS probes the local structure around the selected photo-absorber, in terms of number of neighbouring atoms N , average bond length between absorbing-neighbouring atoms $\langle r \rangle$ and variance σ^2 . Since EXAFS is an element-specific technique, in these systems it is possible to independently achieve information on the individual first nearest neighbours and next nearest neighbours atomic pairs.

3.2 MATERIALS AND EXPERIMENTAL

A CSL sample of $[\text{GeTe} (1 \text{ nm}) / \text{Sb}_2\text{Te}_3 (3 \text{ nm})]_{15}$ with total thickness 60 nm was deposited on Sb-passivated Si(111) surfaces[13], at a substrate temperature of 230 ° C, by means of molecular beam epitaxy (MBE). The film was finally capped to avoid oxidation. The thermodynamically controlled growth has been shown to lead to high-quality superlattices, as in our case.[14; 15] Details about the growth of the CSL sample can be found in the section "Experimental - MBE growth and annealing" of *Momand et al.*[14].

GeTe[16] and Sb_2Te_3 [17] single crystals were used as reference samples.

The high-quality ~ 5 mm size single crystal of Sb_2Te_3 was obtained by slowly cooling a molten stoichiometric mixture of high purity 99.999% of Sb and Te via the Bridgman technique in vertical geometry.[17]

The synthesis of high-quality GeTe single crystal of few mm^2 size was performed by melting the pure elements (Ge,Te) in a vacuum-sealed ampoule, where the proportion was $\text{Te}:\text{Ge}=1.002:1$. The melt was then cooled down and the ampoule end, in the region of the reaction products, was placed for three days in a furnace (at 600° C). The remaining elementary Te evaporated and condensed in the cold end of the ampoule.[16]

EXAFS measurements were performed on two X-Ray Absorption Spectroscopy dedicated beamlines, SAMBA and B18, of SOLEIL Synchrotron (FR) and Diamond

Light Source (UK), respectively. A high photon flux, with nearly constant intensity within the scanned energy range of 11 – 11.8 keV for the Ge K-edge, was provided by a sagittal focusing Si(111) monochromator. By changing the monochromator the available energy range extended to 35 – 40 keV, thus covering also the Sb K-edge. The size of the incident beam on the sample was $22 \times 300 \mu\text{m}^2$. Harmonic rejection was achieved by using two collimating/focusing mirrors (Pt- or Ni-coated). In both beamlines, a Ge detector was used to collect data in fluorescence yield (FLY) mode at room temperature, and the angle of incidence was 50° . Six scans (~ 30 min/scan) per sample were averaged in order to improve the signal-to-noise ratio.[18; 19] At SOLEIL, Bragg peaks from the films and the Si substrates were removed from the CSL absorption spectra by continuously rotating the samples with a spinner.

3.3 RESULTS AND DISCUSSION

3.3.1 Data

EXAFS spectra were processed and analysed using the IFFEFIT package.[20] Background subtraction from raw absorption data $\mu(E)$, conversion to $\chi(k)$, k-weighting and normalization were performed with ATHENA.[20] The relative Fourier Transform magnitudes were obtained using a k-hanning window with $\Delta k = 0.5 \text{ \AA}^{-1}$ of $2.15 - 11.2 \text{ \AA}^{-1}$ and $2.35 - 11 \text{ \AA}^{-1}$ for the Ge and Sb K-edge. In all cases the signal below 1.5 \AA was intentionally suppressed by the RBGK card (see ATHENA manual) since a bond length of atomic pairs could not be smaller than this value. The EXAFS data back Fourier Transforms $\chi(q)$ were extracted applying an R-Hanning window between $2 - 4.5 \text{ \AA}$ and then were fitted with ARTEMIS.[20]

Although the nearby environment of Ge and Sb atoms in the CSL resembles that of bulk GeTe and Sb_2Te_3 , appreciable distortions are observed in particular beyond the first shell.

Left panel of Fig. 7 a shows the Ge K-edge EXAFS data in the photon momentum k range ($0 - 13.5 \text{ \AA}^{-1}$), collected for the bulk GeTe and the CSL samples. The com-

parison reveals a different k -dependent damping and a slight phase shifting of the CSL oscillations with respect to the bulk signal. Such differences can be better appreciated by looking at the EXAFS signals Fourier Transforms (FTs) $|\chi(R)|$ in R -space (right panels of Fig. 7 a). These profiles yield a raw representation of the local structure, where the photo-absorber is centred at $R = 0 \text{ \AA}$. Both the $|\chi(R)|$ spectra display a prominent double peaked feature at $R = 2.7 - 3.2 \text{ \AA}$, stemming from the two photo-electron scattering paths with the first nearest neighbours. In analogy to GeTe single crystal, these paths link Ge to Te atoms. The weaker peaks and shoulders at higher distances can be attributed to the contribution of the next nearest neighbours and multiple scattering effects. In particular, a noticeable difference of the signals in the $3.2 - 5 \text{ \AA}$ radial region reveals a different environment of Ge atoms in the CSL GeTe layers with respect to the stoichiometric GeTe structure. Left panel of Fig. 7 b displays the EXAFS data at the Sb K-edge. A damping-free overlap of the oscillations is visible, leading to a clear proximity in the relative $|\chi(R)|$ profiles of the double peaked structure at $R = 2.9 - 3.2 \text{ \AA}$. Nevertheless, also in this case, the correspondence of the two EXAFS spectra decreases when moving towards higher R . As far as the nearest neighbour spacing is concerned, the similarity of CSL with the corresponding single crystals used for reference (GeTe and Sb_2Te_3) is preserved. Having established a qualitative analysis of the Sb and Ge K-edge $|\chi(R)|$ profiles, it is justified to assume that the average local atomic details of the Ge and Sb photo absorbers in the CSL layers is not exactly compatible with bulk crystalline structure of GeTe and Sb_2Te_3 beyond the nearest neighbour range. The observed differences might help to provide important insights into the atomic arrangement of Ge and Sb atoms in the CSL structure.

3.3.2 TEM Model Structure

In search for a valid structural model of the $[\text{GeTe}/\text{Sb}_2\text{Te}_3]$ interface, the representative crystalline structure revealed by a high-angle annular dark-field imaging scanning TEM study of the CSL sample is considered.[14] Fig. 8 a displays the resulting close-up atomic resolution image with an overlying schematic of the unit cell. This model, herein named Kooi TEM (KT), matches the CSL layered structure reasonably well. In-

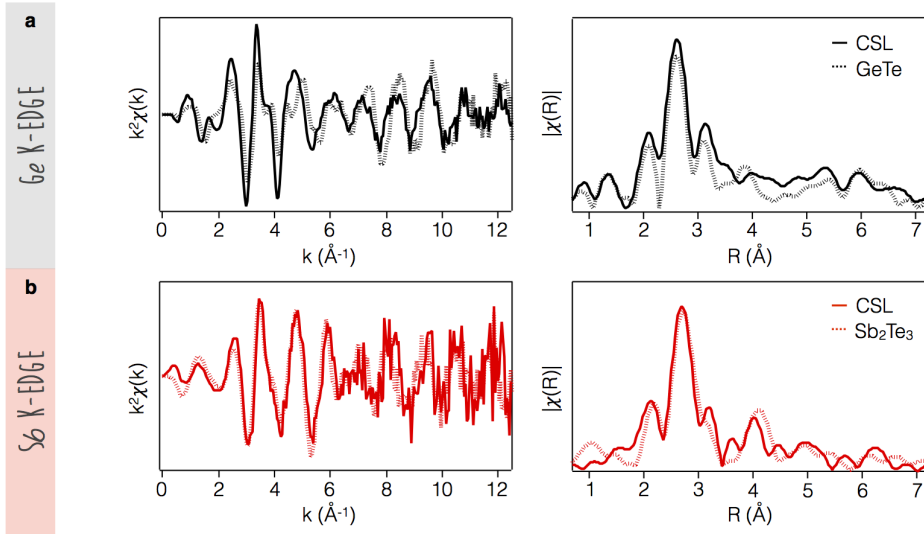


Figure 7: $k^2\chi(k)$ EXAFS signals (left panels) and corresponding Fourier Transform magnitudes $|\chi(R)|$ (right panels) of the CSL sample (continuous curves) and of the reference crystal samples (dashed lines) - GeTe and Sb_2Te_3 , respectively - at: **a** Ge *K*-edge; **a** Sb *K*-edge.

terestingly, the related quantitative investigation on the high-resolution image - black profile[14] - clearly shows two main tendencies: (i) the structure assumes that m GeTe units are intercalated within one single Sb_2Te_3 QL [Te-Sb-Te-Sb-Te], and that the whole block can be coupled via van der Waals (vdW) gaps to $(n-1)$ Sb_2Te_3 QLs, like in natural GST alloys.[21] In particular, here $m = 3$ and $n = 2$; (ii) the external Sb layers in the block are intermixed with Ge atoms, presumably due to inter-diffusion.

3.3.3 Simulations

Based on this structural model for the $[\text{GeTe}/\text{Sb}_2\text{Te}_3]$ stack, $\chi(k)$ signals at the Ge and Sb *K*-edge were computed with an ab-initio approach by means of the FEFF6 code.[20] The simulated spectra were calculated considering all non-equivalent Ge and Sb atomic positions for the absorber and then including single and multiple backscattering paths for a cluster of 8 Å. The pseudo-fitting parameters were set to $S_0^2 = 1$, $\sigma^2 = 0.003$, $\Delta R_{\text{eff}} = 0$, $\Delta E_0 = 0$. Fig. 8 **b** shows the $\text{FT}[\chi(k)]$ moduli on the *R*-space at Ge (black curves) and Sb (red curves) *K*-edge compared to the CSL

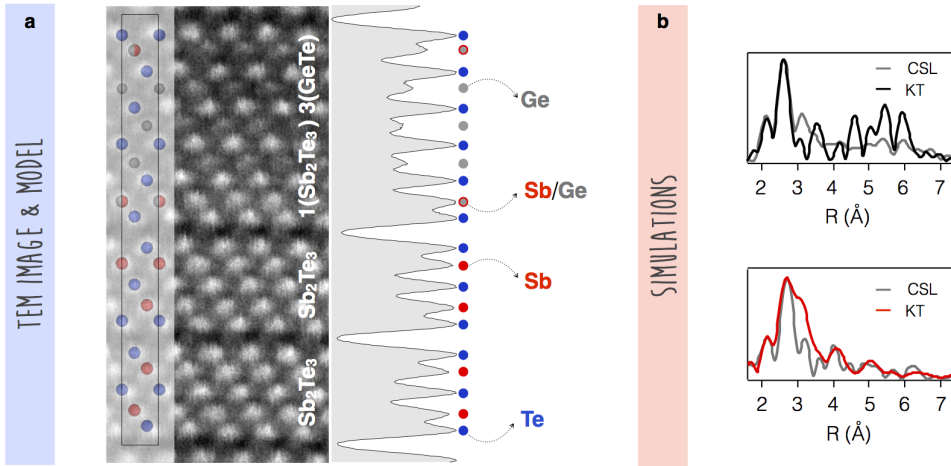


Figure 8: **a** High resolution TEM image of the CSL sample, with overlaid experimental-based averaged structure model. Sb, Te and Ge atoms are denoted with red, blue and grey circles, respectively. Half-colored circles indicate an ideal 50% intermixing of Sb and Ge atoms, as suggested by a quantitative analysis of the present image (black profile). **b** $|\chi(R)|_{exp}$ of the experimental EXAFS data at Ge and Sb K-edge (grey curves) in comparison with the *ab-initio* simulated $|\chi(R)|_{th}$ (Ge-black, Sb-red curves) of the Kooi TEM (KT) model shown in **a**

experimental $|\chi(R)|_{exp}$ spectra (grey curves). The calculated $|\chi(R)|_{th}$ spectra, normalized to the main peak, significantly mirror the main features of the experimental $|\chi(R)|_{exp}$ profiles, up to $\sim 6-7$ Å for both the Ge and Sb K-edge.

For consistency, the simulation was computed also considering four other stacking sequences proposed in literature[7] for similar systems, namely Ferro Ge-Te (F), Petrov (P), Inverted Petrov (IP) and Kooi (K), whose respective unit cells are sketched in Fig. 9 **a** while crystalline parameters are reported in Tab. 1.

All models can be separated into two classes, depending on the character of the separation between the Ge-Te and the Sb-Te layers. The first class presents a full separation of the Ge-Te bilayers moiety from the Sb_2Te_3 quintuple layers (QLs), via weak VdW bonds.[7] The fingerprint of each model is the stacking sequence of the two Ge-Te bilayers. In particular, Ferro-GeTe (F), Petrov (P) and Inverted Petrov (IP) structures have [Ge-Te-Ge-Te], [Ge-Te-Te-Ge] and [Te-Ge-Ge-Te] arrangements, respectively. On the contrary, the second class assumes that m Ge-Te units are inserted into one single Sb_2Te_3 QL [Te-Sb-Te-Sb-Te], and that the whole block can be

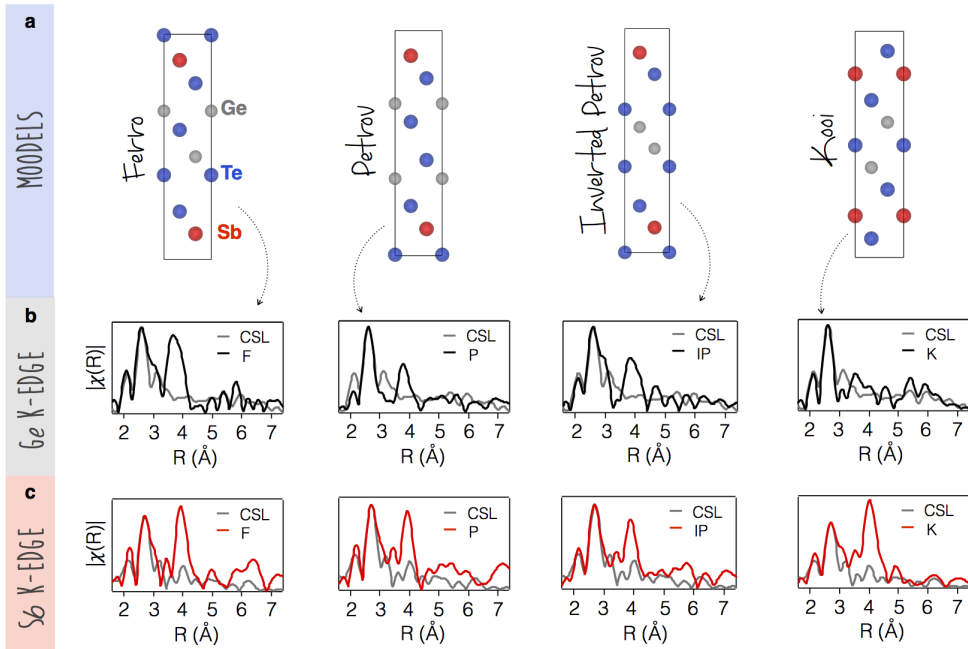


Figure 9: **a** Literature theoretical structures from *Tominaga et al.*[7] and therein. Sb, Te and Ge atoms are denoted with red, blue and grey circles, respectively. **b** $|\chi(R)|_{exp}$ of the experimental EXAFS data at Ge and Sb K-edge (grey curves) in comparison with the *ab-initio* simulated $|\chi(R)|_{th}$ (Ge-black, Sb-red curves) of the four models shown in **a**.

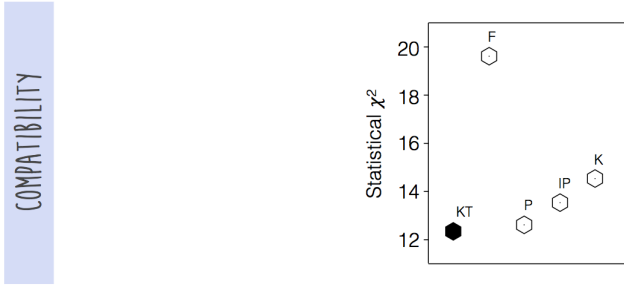


Figure 10: Statistical χ^2 -values from a comparison between theoretical models[7] and experimental CSL data.

joined via VdW gaps to $(n-1)\text{Sb}_2\text{Te}_3$ QLs, like in standard GST alloys.[21] The Kooi (K) model belongs to this class and has $m=2$ and $n=1$.

Fig. 9 b,c displays the $|\chi(R)|_{th}$ simulated spectra for each model compared with the $|\chi(R)|_{exp}$ profiles -normalized to the main peak- at the Ge and Sb K-edges.

Although these simulations are affected by the unavoidable approximation of the *ab-initio* calculation, a good agreement between all the models and the experimental data is appreciable as far as the first nearest neighbour range is taken into account. On the other hand, it is to be noted that the second and third neighbour structure (above 3 Å.) plays a crucial role in distinguishing the models. Thus, a χ^2 comparison was implemented with an IGOR pro built-in function[22], yielding an estimate of how representative a single model is with respect to the experimentally observed structure. The χ^2 values relative to the two K-edges were summed up for each model-experiment pair in order to obtain a correlation. The results of this analysis are reported in Fig. 9 d. The KT model has the lowest χ^2 value and, interestingly, the χ^2 value provided by the Petrov (P) model is also close to the minimum. This is probably due to the fact that this structure can be viewed as a KT stacking sequence with an extra Ge layer between the two central Te layers (Fig. 10). Consequently, the comparison discussed above suggests that the KT structure, being experimental-based and being noticeably more consistent at high R-values with respect to the other models, is a good starting point for a refinement of the quantitative EXAFS fitting analysis.

| | a (Å) | c (Å) | χ^2 |
|----------------------|---------|---------|----------|
| Ferro-GeTe (F) | 4.23 | 19.14 | 19.61 |
| Petrov (P) | 4.27 | 17.70 | 12.63 |
| Inverted Petrov (IP) | 4.23 | 18.71 | 13.55 |
| Kooi (K) | 4.12 | 17.20 | 14.52 |
| Kooi TEM (KT) | 4.25 | 41.26 | 12.34 |

Table 1: Crystalline parameters a and c of: (i) the theoretical models as in *Tominaga et al.*[7]; (ii) the experimental TEM averaged structure as in *Momand et al.*[11] χ^2 values from a comparison between theoretical models[7] and experimental CSL data.

3.3.4 Wavelet Analysis

Furthermore, in order to corroborate the qualitative observations of the raw data and of the χ^2 comparison, a continuous wavelet transform (WT) analysis[23] on the CSL and GeTe samples at the Ge K-edge was computed. The WT analysis is able to resolve the k -dependence of the absorption signal, having a simultaneous resolution in R -space. In this way, the contribution from atoms of different elements at the same distance from the absorber can be in principle distinguished.

The Wavelet Transform (WT) is a mathematical complete transformation of a signal. Regarding a k^3 -weighted EXAFS data, the expression of the WT is given by:

$$W_f^\psi(r, k) = \sqrt{2r} \int_{-\infty}^{+\infty} \chi(k') k'^3 \psi^*[2r(k' - k)] dk'$$

where r corresponds to the abscissa of the FT of the EXAFS signal ($\chi(k')$) and $\psi^*[2r(k' - k)]$ is the wavelet mother function. In particular, ψ is the Morlet function, which is a complex sine wave confined in a Gaussian envelope:

$$\psi(t) = \frac{1}{\sqrt{2\pi\sigma}} (e^{i\eta t} - e^{-\eta^2 \sigma^2/2}) e^{-t^2/2\sigma^2}$$

The parameter η is the frequency of the sine or cosine function, defining how many oscillations there are in a Gaussian envelope with FWHM of σ . [23] All computations were accomplished with the IGOR program for the WT analysis, written by Dr. M.

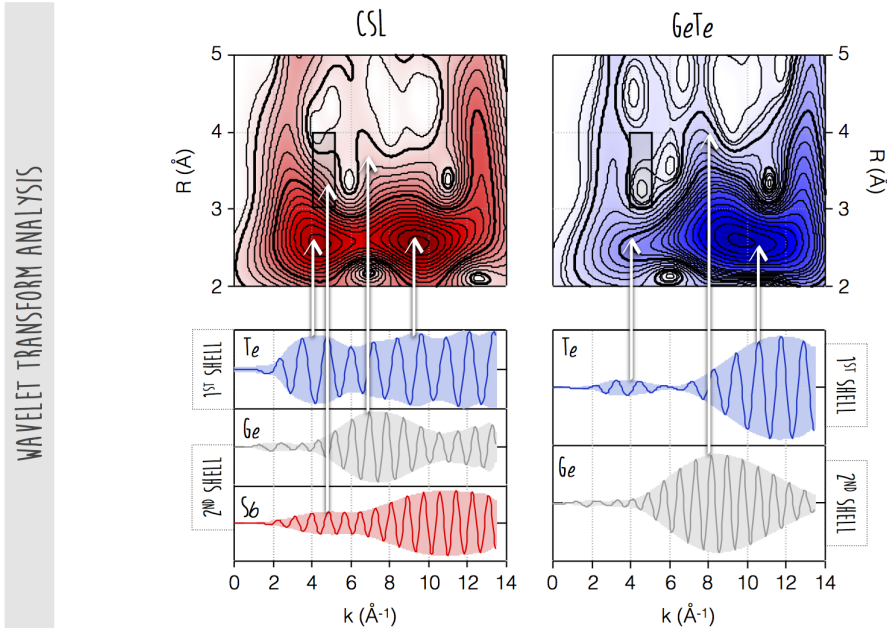


Figure 11: Upper panels: 2D plot of the Morlet Wavelet-Transform analysis. **Lower panels:** simulation of the backscattering paths corresponding to the 1st and 2nd shells, for the KT and the GeTe single crystal[25] models. Vertical dashed lines are guides to the eye. The maxima of the envelope of the model backscattering signals contribute to specific regions (black boxes) of the experimental WT. The comparison with the model signals helps to decompose the experimental WT.

Chukalina and Dr. H. Funke.[24] In order to obtain a very high resolution in k-space rather than in R-space, η was fixed to 30 and σ to 0.25 .

The upper panels in Fig. 11 show the resulting 2D plot of the WT analysis, using k^3 -weighted spectra and a Morlet function as kernel. It is to be noted that, at a first glance, the main difference between single crystal reference and superlattice signals output is visible in the radial region corresponding to the first shell, namely 2–3 Å. Two contributions at 4 Å⁻¹ and 10 Å⁻¹ are clearly resolved in the CSL, while in GeTe the first ridge is less intense. Moving towards the second shell radial region 3–4 Å, a shoulder appears between 4–6 Å in CSL, replacing the intensity-hole present in GeTe. In order to understand these qualitative differences, simulations of the backscattering paths $\chi(k)$ signals corresponding to the first and second shells were performed, according to the method above mentioned. For CSL and for

GeTe the KT model and the structure described by *Nonaka et al.*[25] were used, respectively. Fig. 11 lower panels display these simulations. The dashed vertical lines associate the peaks of the various k^3 -weighted $\chi(k)$ envelopes to the region with corresponding intensity in the 2D WT map. Regarding the first shell, the envelope amplitudes match with experimental data. The difference between CSL and GeTe, can be ascribed to the inclusion of multiple FEFF calculations referred to non-equivalent Ge sites for CSL, rather than of the single one for GeTe case. Therefore, more than one type of Te local environment with respect to Ge atoms might be present. Focussing on the second shell, in particular where appreciable dissimilarities with the GeTe case are visible, the contributions of Ge-Ge backscattering paths agree in both images. Interestingly, the intensity hole observed in the momentum-distance grey box $(4 - 5.5 \text{ \AA}^{-1}) \times (3 - 4 \text{ \AA})$ of the single crystal case is completely filled for the CSL case. Important to note is that, by looking at the simulated profile of Sb neighbouring atoms, a peak of the envelope is visible at low k values. Therefore, this observation upon a simple change on the visualization of the raw data can help in identifying the presence of a backscatter element different from Ge and Te in the next nearest neighbours environment of Ge absorbing atoms.

3.3.5 Fitting Procedure

The experimental-based KT model (shown in details in Fig. 13 a) was used to fit the back FT of the CSL sample EXAFS $\chi(k)$ oscillations (Fig. 12). In the single building-block, made up of 3 GeTe BLs intercalated within 1 Sb_2Te_3 QL, the Sb-layers locate preferentially close to the edges.[21] Here, these Sb-layers are considered with an ideal 50% intermixing of Ge atoms, schematized in Fig. 13 a with half-colored balls. Henceforth the following nomenclature will be used for recalling the atomic positions in the unit cell as depicted in Fig. 13 a: (i) A site, for Ge or Sb atoms in the center of their respective building-block (GeTe or QL); (ii) B site, for Ge atoms close to the intermixed layer in the main building-block; (iii) C site, for Ge or Sb atoms in the intermixed layer.

The procedure employed a linear combination of theoretical backscattering paths generated with FEFF6[20], making use of 7 \AA clusters of the KT model[14]. Single

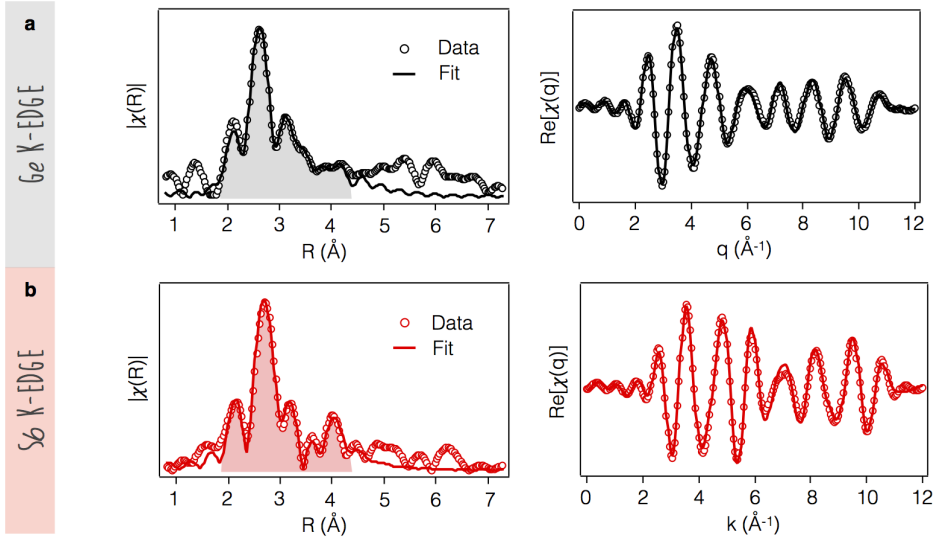


Figure 12: a FTs moduli (left panels) and (right panels) back FT real parts of the experimental EXAFS profiles at Ge and Sb *K*-edge of CSL and best fit results. Shaded-grey and -red regions corresponds to the R-hanning window (1.9–4.5 Å) considered for the back FT extraction and fitting.

scattering paths with R_{eff} up to 4.5 Å and with a theoretical scattering amplitude higher than the 10% with respect to the first path, were included. According to the atomic element populations in the unit cell, the FEFF calculations relative to A, B and C atomic sites were included in the procedure, with different weights. In order to improve the fitting reliability and to decrease the number of degrees of freedom, a co-refinement procedure of the CSL experimental data at Ge and Sb *K*-edge was performed, using the ARTEMIS code.[20] In particular, for a given Ge-Sb bond its theoretical radial distance R_{eff} and its relative Debye-Waller factor σ^2 were assumed to vary alike, regardless of which was the absorber. For each edge, one amplitude reduction term S_0^2 and one inner potential correction ΔE_0 were considered. The number of neighbours N was constrained by the degeneracy values based on the symmetry of the KT model structure. In addition, the fit was performed in parallel with three different k -weights (1, 2 and 3), in order to tackle both contributions at low and high k -values. Therefore, the EXAFS results could be obtained more reliably not only for the first nearest neighbour pairs, but also for the second nearest neighbours pairs.

Fig. 12 shows the Ge (black) and Sb (red) K-edge spectra and their best fits in q (right panels) and R (left panel)s space. The R_{factor} represents a measure of a fit effectiveness, being the sum of the square of the residuals between measured and model data, normalized to the magnitude of the experimental data. Furthermore, distances with a separation higher than $\delta R = \pi/2k_{max}$ can be resolved by EXAFS spectroscopy.[26] In the CSL case of our investigation, $R_{factor} = 0.0087$ and the experiment resolution is given by $\delta R = 0.14 \text{ \AA}$.

Tab. 2 lists the interatomic distances of CSL, as a result of the co-refinement fitting procedure with the KT structure model. Two concentrically coordinated spheres surrounding the Ge and Sb absorbers with different radii were identified. The first shell includes the short and long out-of-plane bonds between the absorbers and the Te atoms, which are schematized in Fig. 11 c. A quick look at the interatomic distances in Tab. 2 indicates the presence of structural distortions with respect to the bulk parent compounds. While Sb sites, regardless of the Sb atomic position, tend to keep a robust environment similar to that of bulk Sb_2Te_3 , Ge sites show increasing distortion depending on the distance from the interfacial layer. Regarding the first shell distances, as shown in Tab. 2, all the Sb-Te distances have a strong similarity with bulk Sb_2Te_3 (see Appendix 3.4 for reference), within the experimental error uncertainty. On the contrary, for the Ge-Te distances three non-equivalent Ge sites were observed. In particular, A-Ge presents a 6-fold symmetry that is lost in the other two cases; B-Ge has a bulk GeTe correspondence (see Appendix 3.4 for reference). Interesting to note is that C-Ge resembles instead the Sb-Te distances in the QLs. The second shell is composed by the in-plane and out-of-plane bonds of the absorbers with Ge and Sb atoms, which are schematized in Fig. 13 b. X-X defines the pairs Ge-Ge, Ge-Sb and Sb-Sb. The in-plane distance ($X-X_{in-p}$) coincides with the lattice parameter of the CSL unit cell for all layers. The resulting value is smaller than the single crystal references ones. Essentially, except for the central A-Ge, the second shell distances are consistent with bulk Sb_2Te_3 . The Ge-Te and Ge-Ge planes in the CSL internal block are slightly vertically closer than in bulk GeTe. The intermixed Sb(Ge) layers preserve the distances as in QLs. The distortions observed on the CSL structure suggest that the physical properties, and in particular the bonding character, is substantially different from what predicted by idealized CSL. The observation of three

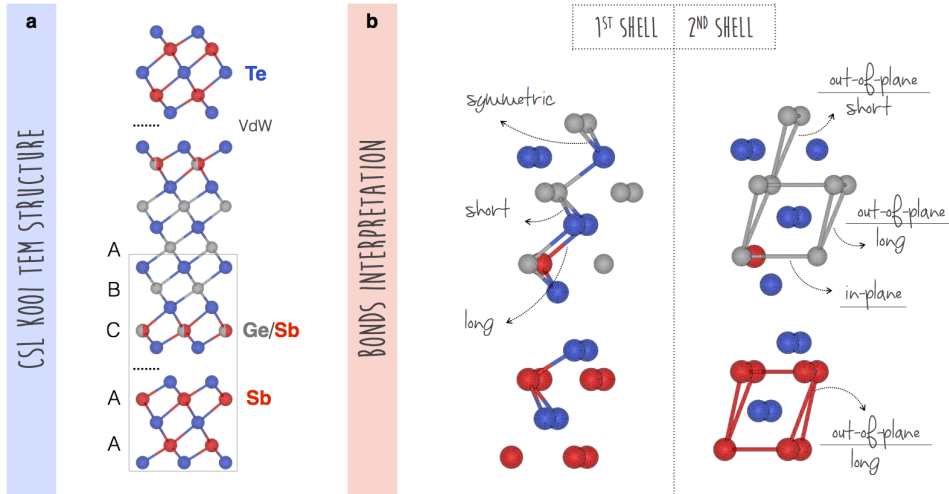


Figure 13: **a** View of the average structure model KT used in the fitting procedure. It presents an ideal 50% intermixing with Ge atoms in the Sb layer in front of the QLs. In particular, the marked Sb and Ge atoms represent the different absorber inequivalent positions A, B and C. **b** Close-up of the grey-box zone **a** with highlighted distances relative to the 1st and 2nd shells, respectively.

different types of Ge sites implies that also their chemical bonding is different. The undistorted 6-fold Ge-Te bonding is in strict contrast with the GeTe bulk case where Peierls distortions form distinct shorter and longer bonds. This observation opens up a scenario where the undistorted GeTe site in the CSL structure determines a pronounced electron delocalisation and 0 energy gap at E_F which characterises resonant bonding.[27; 28] Such an atomic structural evidence could also rationalise the observed metallic state of our CSL samples. The distorted B and C Ge sites may lead to a significantly increased electronic static polarizability and in turn to a ferroelectric response.

3.4 CONCLUSIONS

Finally, a representative high-quality $[\text{GeTe} (1 \text{ nm}) / \text{Sb}_2\text{Te}_3 (3 \text{ nm})]_{15}$ superlattice sample is probed by means of EXAFS spectroscopy to unveil the as-grown crystalline state structure at the interface of the two materials. The observed distortion

| 1 st Shell | | N | R(Å) | σ^2 (Å ²) |
|----------------------------------|-------|----|---|------------------------------|
| Ge-Te _{short} | A | 6 | 2.85(1) | 0.011(1) |
| | B | 3 | 2.81(1) | 0.011(1) |
| | C | 3 | 2.93(1) | 0.011(1) |
| Ge-Te _{long} | B | 3 | 3.09(2) | 0.012(2) |
| | C | 3 | 3.15(2) | 0.012(2) |
| Sb-Te _{short} | A | 6 | 2.95(1) | 0.008(1) |
| | C | 3 | 2.93(2) | 0.008(1) |
| Sb-Te _{long} | A | 3 | 3.13(3) | 0.014(1) |
| | C | 6 | 3.16(3) | 0.014(1) |
| 2 nd Shell | | N | R(Å) | σ^2 (Å ²) |
| Ge-Ge _{out-p, short} | | 9 | 3.94(3) | 0.011(5) |
| X-X _{in-p} | Ge-Ge | 14 | 4.17(3) | 0.009(4) |
| | Ge-Sb | 8 | 4.17(3) | 0.009(4) |
| | Sb-Sb | 14 | 4.17(3) | 0.014(8) |
| X-X _{out-p, long} | Ge-Ge | 5 | 4.39(4) | 0.006(2) |
| | Ge-Sb | 4 | 4.39(4) | 0.003(1) |
| | Sb-Sb | 6 | 4.39(4) | 0.013(5) |
| Other Parameters | | | | |
| R _{factor} (Ge)= 0.0036 | | | S ₀ ² (Ge)= 0.78(4) | |
| R _{factor} (Sb)= 0.011 | | | S ₀ ² (Sb)= 0.8(1) | |

Table 2: Interatomic distances and local structure parameters relative to 1st and 2nd shell of CSL, as a result of the co-refinement fitting procedure -uncertainties are included in parentheses. The atomic positions are identified with A, B and C, as depicted in Fig. 13 a. X-X defines the pairs: Ge-Ge, Ge-Sb and Sb-Sb. It is important to note that the degeneration N of the bonds in the 2nd shell is the sum of degenerations for each different inequivalent site position of Ge and Sb.

of the lattice, the vdW gap shift and the Ge(Sb) intermixing should be considered as worthwhile features of these as-grown CSLs, since they would possibly affect the phase-change performances, in terms of electrical switching and activation energy. In this regard, our results - combining an optimized growth process and a careful atomistic structural characterization - prospect for CSLs a phase-change mechanism more complex than a oversimplified atomic Ge flipping.

3.5 APPENDIX: ATOMIC STRUCTURE OF BULK MATERIALS

For reference, the following structural models were used in order to fit the EXAFS data of bulk materials at Ge and Sb K-edge: (i) for GeTe - Space group R3m, $a = 4.281 \text{ \AA}$ [25], (ii) for Sb_2Te_3 - Space group R-3m, $a = 4.25 \text{ \AA}$ [29]. Also here, the procedure employed a linear combination of theoretical backscattering paths generated with FEFF6[20], making use of 7 Å clusters of the above cited models[25; 29]. Single scattering paths with R_{eff} up to 4.5 Å and with a theoretical scattering amplitude higher than the 10% with respect to the first path, were included. The fitting procedures on the single crystals provided results in good agreement with literature.[6; 26; 30; 31] Best fit values of structural parameters obtained by EXAFS analysis are reported together with their uncertainties in Tab. 3.

| GeTe | N | R(Å) | σ^2 (Å^2) |
|-------------------------------------|---|-------------------|-----------------------------|
| Ge-Te _{short} | 3 | 2.80(1) | 0.007(1) |
| Ge-Te _{long} | 3 | 3.14(1) | 0.013(1) |
| Ge-Ge _{out-p} | 6 | 4.12(1) | 0.016(3) |
| Ge-Ge _{in-p} | 6 | 4.30(1) | 0.016(4) |
| $R_{\text{factor}} = 0.0032$ | | $S_0^2 = 0.45(2)$ | |
| Sb₂Te₃ | N | R(Å) | σ^2 (Å^2) |
| Sb-Te _{short} | 3 | 2.95(2) | 0.009(2) |
| Sb-Te _{long} | 3 | 3.10(3) | 0.015(7) |
| Sb-Sb _{in-p} | 6 | 4.20(3) | 0.014(6) |
| Sb-Sb _{out-p} | 6 | 4.32(6) | 0.012(8) |
| $R_{\text{factor}} = 0.0062$ | | $S_0^2 = 0.65(7)$ | |

Table 3: Local structure parameters for single crystal GeTe and Sb_2Te_3 . Uncertainties are included in parentheses.

BIBLIOGRAPHY

- [1] T. C. Chong, L. P. Shi, R. Zhao, et al. *Applied Physics Letters*, 88(12):122114, 2006.
- [2] T. C. Chong, L. P. Shi, X. Q. Wei, et al. *Physical Review Letters*, 100:136101, 2008.
- [3] C. Chia Tan, L. Shi, R. Zhao, et al. *Applied Physics Letters*, 103(13):133507, 2013.
- [4] P. Long, H. Tong, and X. Miao. *Appl. Phys. Expr.*, 5(3):031201, 2012.
- [5] R. E. Simpson, P. Fons, A. V. Kolobov, et al. *Nature Nanotechnology*, 6(8):501–505, 2011.
- [6] D. Bang, H. Awano, J. Tominaga, et al. *Scientific Reports*, 4(5):426–432, 2014.
- [7] J. Tominaga, A. V. Kolobov, P. Fons, T. Nakano, and S. Murakami. *Advanced Materials Interfaces*, 1(1):1300027, 2013.
- [8] X. Yu and J. Robertson. *Scientific Reports*, 5:12612, 2015.
- [9] J. Tominaga, P. Fons, A. Kolobov, et al. *Jpn. J. Appl. Phys.*, 47(7S1):5763, 2008.
- [10] J. Tominaga, T. Shima, P. Fons, et al. *Jpn. J. Appl. Phys.*, 48(3S1):03A053, 2009.
- [11] J. Momand, R. Wang, J. E. Boschker, et al. *Nanoscale*, 7:19136–19143, 2015.
- [12] S. Raoux and M. Wuttig. *Phase Change Materials*. Springer US, 2008.
- [13] R. Wang, J. E. Boschker, E. Bruyer, et al. *The Journal of Physical Chemistry C*, 118(51):29724–29730, 2014.
- [14] J. Momand, R. Wang, J. E. Boschker, et al. *Nanoscale*, 7:19136–19143, 2015.
- [15] J. E. Boschker, J. Momand, V. Bragaglia, et al. *Nano Letters*, 14(6):3534–3538, 2014.
- [16] M. Leszczynski, A. Szczerbakow, and G. Karczewski. *Journal of Crystal Growth*, 135(3–4):565 – 570, 1994.
- [17] J. C. Johannsen, G. Autès, A. Crepaldi, et al. *Physical Review B*, 91:201101, 2015.
- [18] V. Briois, E. Fonda, S. Belin, et al. SAMBA: The 4–40 keV X-ray absorption spectroscopy beamline at SOLEIL. In C. M. e. S. F. E. A. Calisti, editor, *UVX 2010 - 10e Colloque sur les Sources Cohérentes et Incohérentes UV, VUV et X ; Applications et Développements Récents*, pages 41–47, 2011. doi: 10.1051/uvx/2011006.

- [19] A. J. Dent, G. Cibir, S. Ramos, et al. *JPCS*, 430(1):012023, 2013.
- [20] B. Ravel and M. Newville. *Journal of Synchrotron Radiation*, 12(4):537–541, 2005.
- [21] J. L. F. Da Silva, A. Walsh, and H. Lee. *Physical Review B*, 78:224111, 2008.
- [22] IGOR Pro 6.3 - Available at: <http://www.wavemetrics.com>, 2018.
- [23] H. Funke, M. Chukalina, and A. C. Scheinost. *Physical Review B*, 71:094110, 2005.
- [24] M. Chukalina and H. Funke. Wavelet transform software, 2016. www.esrf.fr/exp-facilities/BM20/Software/Wavelets.html.
- [25] T. Nonaka, G. Ohbayashi, Y. Toriumi, Y. Mori, and H. Hashimoto. *Thin Solid Films*, 370(1-2):258–261, 2000.
- [26] A. N. Mansour, W. Wong-Ng, Q. Huang, et al. *Journal of Applied Physics*, 116(8):083513, 2014.
- [27] K. Shportko, S. Kremers, M. Woda, et al. *Nature Materials*, 7(8):653–658, 2008.
- [28] L. Pauling. *The Nature of the Chemical Bond*. Cornell University Press, Ithaca, NY, 1939.
- [29] T. L. Anderson and H. B. Krause. *Acta Crystallographica B*, 30(5):1307–1310, 1974.
- [30] P. Fons, A. V. Kolobov, M. Krbal, et al. The phase-transition in GeTe revisited: Local Versus Average Structure. In *European Phase Change and Ovonic Symposium - EPCOS*, 2010.
- [31] K. Tani, N. Yiwata, M. Harigaya, S. Emura, and Y. Nakata. *Journal of Synchrotron Radiation*, 8(2):749–751, 2001.

4

SINGLE-SHOT AMORPHIZATION OF GST NANOPARTICLES

ABSTRACT¹

In this Chapter we show the experimental optical crystalline-to-amorphous transition of $\text{Ge}_2\text{Sb}_2\text{Te}_5$ nanoparticles by using a single-shot laser pulse, satisfying a mandatory requirement of a bit-memory element. We demonstrate that 0-dimension confinement results in a drastic reduction of the minimum critical fluence required for optical-induced amorphization when compared to thin-film cases. These unprecedented results open a viable route to boost energy efficient phase-change processes and thus suggest nanoparticles as promising option for tailoring successful optoelectronic devices.

After a brief introduction to the main recent advances in the field, the first part of this Chapter is devoted to the presentation of the experimental raw data and the related quantitative analysis. Later on, additional structural and optical measurements will support a coherent and thorough interpretation our results. Finally, the advantages and potentials of the nanoparticle-systems will be discussed in details.

¹This chapter has originally been published as Casarin B. et al., *Ultralow-Fluence Single-Shot Optical Crystalline-to-Amorphous Phase Transition in Ge-Sb-Te Nanoparticles*, *Nanoscale*, 10, 16574, (2018).

4.1 RECENT ADVANCES AND MAIN CONTEXT

Optical single-shot stable amorphization has been induced in $\text{Ge}_2\text{Sb}_2\text{Te}_5$ films with different thicknesses.[1–5] A single fs-pulse is sufficient to initiate laser-amorphization, as it generates suitable conditions for sudden high energy deposition followed by an ultrafast super-cooling.[4]

Nanoparticles (NPs) offer several potential advantages to the RESET (crystalline-to-amorphous) process.

Firstly, NPs have a lower melting temperature with respect to the bulk parent compounds. In particular, there is a close dependence of the melting point on the inverse of the particle size:[6; 7]

$$T_{\text{melt,NPs}} = T_{\text{melt,bulk}}[1 - (c/d)^n] \quad (7)$$

where c is a material-dependent parameter, d is the nanoparticle diameter and $n=1, 2$ for metal[6] or semiconductors[7], respectively.

Secondly, NPs guarantee the highest cooling rate with respect to larger bulk structures, because of the high surface-to-volume ratio. It is important to note that these are intrinsic properties attributed both to a single and a group of NPs.

In line with these remarks, by suitable choices of the substrate/capping materials and of the optical light, it is possible to further improve the heating process, thus reducing the energy needed to heat the NPs. Thus, this kind of low-dimensional system offers an extremely interesting playground to investigate and optimize the RESET process in PCMs. The above considerations define our dimensional strategy of focussing on 0-D GST systems.

4.2 SAMPLE DETAILS

GST stoichiometric amorphous NPs ($\text{Ge:Sb:Te}=20:23:57(1)$ at%) with diameter ~ 7.4 nm and ~ 10.8 nm were deposited on Mica substrates, adopting magnetron sputtering

technique combined with inert gas condensation in ultra high vacuum. A small amount of methane was incorporated during NPs deposition to form the nascent clusters. Details of NPs deposition can be found elsewhere.[8]. Transmission Electron Microscopy revealed the monodisperse size distribution of the produced NPs (± 1 nm), as well as their amorphous nature. Crystallization was achieved right after the deposition by annealing the GST amorphous NPs at 465 K for 10 min in vacuum at 10^{-2} mbar.[8] The crystalline structure of the different size NPs was checked by HRTEM *in situ* diffraction. Accordingly, it was found a mixture of two phases, namely the fcc (Fm-3m) rock-salt and the hexagonal ones. Impurities on the surface of these NPs, in the form of a thin oxide shell, prevent coalescence. As proof, Fig. 14 shows a bright field HRTEM image of crystalline GST NPs with diameter size 10.8 ± 1.0 nm. The measurement was performed on a JEOL 2010 at 200 kV. Due to the visible high coverage of the substrate (95%), it is possible to note that the NPs can overlap but are still decoupled from each other. Thus, the sample consists of individual particles. NPs were then capped *ex-situ* with 200 nm polymethyl metacrylate. Thus, the “pristine” (i.e. not yet laser-treated) samples are crystalline $\text{Ge}_2\text{Sb}_2\text{Te}_5$ NPs, herein named GST NPs. The choice of limiting our investigation over the $\sim 7 - 11$ nm NPs is twofold. Firstly, we restricted to a NPs dimension range with similar optical response in the wavelength range of interest, where -for instance- the Rayleigh condition is still valid. The second point stems from the necessity of an uniform heating of the NPs after the laser pulse arrival. This condition is of uttermost importance in order to avoid possible phase-mixing, partial melting, etc. Accordingly, the NPs dimension must be of the same order of the optical penetration depth (~ 20 nm at 400-800 nm).

4.3 EXPERIMENTAL RESULTS

Fig. 15 displays optical microscope images of a complete series of single-shot excited areas as a function of increasing laser energy (top rows, for both NPs diameters). This series was iterated four times per sample (see ESI Video, available at [Nanoscale website](#)). Below a pulse energy of $0.1 \mu\text{J}$, no transmittivity change is visible on the NPs samples. Between 0.1 and $0.6 \mu\text{J}$ elliptical homogeneous spots form and appear

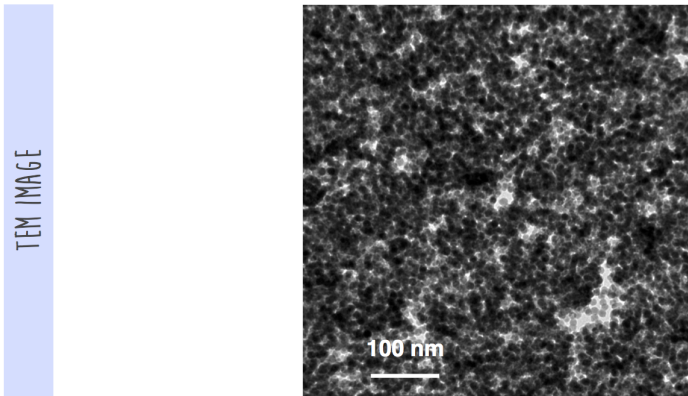


Figure 14: TEM image of 10.8 ± 1.0 nm $\text{Ge}_2\text{Sb}_2\text{Te}_5$ NPs before the deposition of the PMMA capping layer.

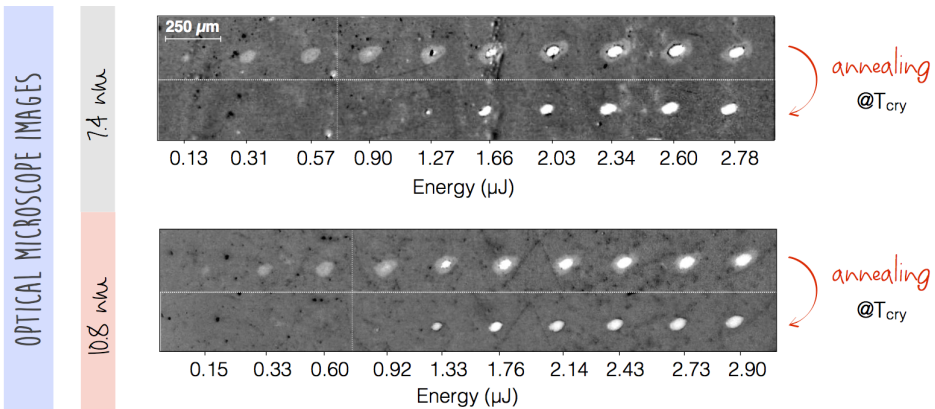


Figure 15: Optical microscope images of 80 fs-single shot laser spots obtained with increasing (left to right) pump energy for the two dimensions NPs (7.4 nm left, 10.8 nm right), before (upper panels) and after (lower panels) annealing above T_{cry} .

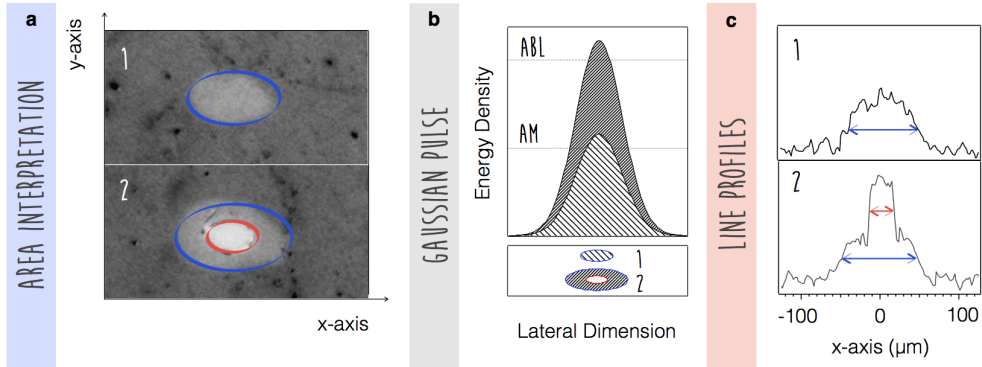


Figure 16: **a** Close-up images of: **1** amorphized, **2** amorphized and ablated marks. **b** Model of the pump pulse with gaussianized shape and theoretical related in-plane projected effects on the NPs, according to the pulse energy density. **c** Example of (1) $\sim 0.6 \mu\text{J}$ and (2) $\sim 1.3 \mu\text{J}$ marks spatial profile, seen as a transmission variation along the x-axis. The red and blue lines correspond to the ablated and amorphized diameters of the spots along the x-axis, respectively.

to be brighter than the uniform crystalline background, as also shown in the close up image of Fig. 16 a panel 1. Above $0.6 \mu\text{J}$, two distinct regions can be identified within the excited spots area, as displayed in panel 2 of Fig. 16a: (i) an outer ring and (ii) an inner core. Thermal annealing at $T_{\text{cry}} = 425 \text{ K}$ for 15 min[8] uncovered the reversible character of the homogeneous elliptical and annular regions towards the crystalline background, as shown in Fig. 15 (bottom rows, for both NPs diameters). On the contrary, the inner cores lasted. The observed optical contrast in the VIS range and the result of thermal annealing are the first qualitative signatures of amorphous GST (elliptical spots and external annuli) and ablated (inner cores) states production. In addition, the radii of both ablated and amorphized spots increase with increasing pump energy.

All these effects can be explained by considering the laser pulse gaussian shape and the related energy density profile distribution within. Fig. 16 b sketches the optical pulse shapes with increasing energy density along with the corresponding in-plane projections. Accordingly, the amorphization and ablation occur in regions where the energy density exceeds specific thresholds.

To estimate these thresholds, a geometrical analysis of the laser marks produced on the NPs samples is carried out. We performed a line-profile study of the single-

shot areas to disentangle regions with different VIS light transmission through the sample. Fig. 16c displays an example of the line-profile along the x-axis of the spot obtained with a laser pump energy where only amorphization (panel 1) or both amorphization and ablation occur (panel 2). In particular, in panel 2 high intensity transmission at the center of the spot can be ascribed to ablation, while the lateral shoulders with an intermediate intensity are related to the amorphization process. The spots diameters are taken at half of the transmission rising edges. In Fig. 16c, the blue and red horizontal lines identify the dimensions of the same-color ellipses in the nearby close-up image of Fig. 16a. Consequently, it was possible to calculate the effective marked spot areas. The pulse energy profile at the focus can be described as a 2-D gaussian function:[2; 9]

$$E(x, y) = E_0 e^{-\left[\left(\frac{x}{w_x/\sqrt{2}}\right)^2 + \left(\frac{y}{w_y/\sqrt{2}}\right)^2\right]} \quad (8)$$

where E_0 is the laser energy density at maximum and w_x, w_y are the $1/e^2$ radii along the two principal axes. The parameter $p^2 = \left(\frac{x}{w_x/\sqrt{2}}\right)^2 + \left(\frac{y}{w_y/\sqrt{2}}\right)^2$ identifies the laser intensity *level curves* and denotes an ellipse with radii $pw_x/\sqrt{2}, pw_y/\sqrt{2}$ and area $\pi p^2 w_x w_y/2$. Thus, a critical threshold energy E_C (in our case for amorphization “AM” or ablation “ABL”) is linked to the critical parameter p_C via the relation $E_C = E_{C,0} e^{-p_C^2}$. The critical area A_C relating the spot dimension with the laser intensity can then be rewritten as:[2; 9]

$$A_C = \frac{\pi}{2} w_x w_y \left[\ln(E_{C,0}) + \ln\left(\frac{1}{E_C}\right) \right] \quad (9)$$

The computed amorphized and ablated areas are shown in Fig. 17 as a function of the laser pump energy. The horizontal error-bars were determined during the pump energy calibration process and correspond to $\pm 0.05 \mu\text{J}$. At low fluences and above a threshold value, the marks area increases rapidly, reaching almost a saturation regime above $\sim 2.5 \mu\text{J}$. Equation 9 properly describes the data. These trends are resolved by a simple fitting where the parameters are $\alpha = \frac{\pi}{2} w_x w_y$ and $\beta = \ln(1/E_C)$.

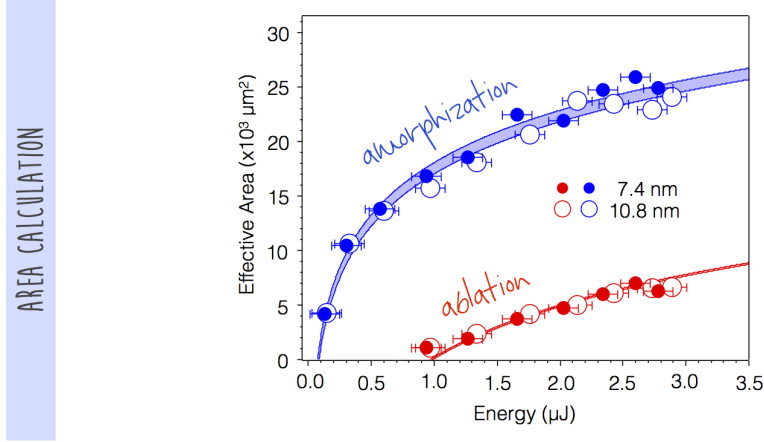


Figure 17: Amorphized and ablated area trend as a function of the pump energy. The fitting function is given by Eq. 9.

Since α is a parameter referred to the laser spot size, it must be independent from the laser energy. Thus, we performed a simultaneous fitting procedure of the four trends by keeping the same α value in all cases. We obtained $\alpha = 6900 \mu\text{m}^2$. The values w_x and w_y measured with the cutting edge yield an area 20 % larger than the one deduced from the fit, yet corresponding just to a 10 % difference in the determination of the spot linear dimensions. Once the spot dimensions are fixed, it is possible to obtain the critical average fluence $F_{avg} = E_{AM}/(\pi w_x w_y)$ by substituting the fit parameters in the relation $e^{-\beta}/(2\alpha)$. In the limit of amorphizing a single NP (abscissa intercept with ordinate 0-level in Fig. 17), the threshold fluence must correspond to the maximum fluence $E_{0,max} = 2F_{avg}$ occurring at the center of the spot.

4.3.1 Thermodynamics

The interaction between a laser pulse and a spherical nanoparticle is characterized by three parameters: (i) the pulse duration; (ii) the heat absorption and (iii) the heat conduction.[10] The typical time for particle-medium heat exchange is given by $t_T \sim (d/2)^2/4\chi$, where χ is the thermal diffusivity of the surrounding medium. In our case, either substrate and capping layer materials present a substantially similar thermal diffusivity (1.4×10^{-7} and $1.95 \times 10^{-7} \text{ m}^2/\text{s}$ for PMMA[11] and Mica[12], re-

spectively). Therefore, in first approximation, $t_T \sim 30$ ps. Since our pulse duration $t_p = 80$ fs is much lower than this characteristic time, we can assume that -during a single pulse event- the heat is absorbed and totally confined in the nanoparticle, which reaches T_{max} , exceeding -in some cases- even the melting temperature.[10] After t_T , a substantial heat amount is deposited in the nanoparticle neighbouring medium. In particular, an ideal outer shell -with thickness equal to the nanoparticle radius- warms up to $T_{max}/2$.[10]

Accordingly, we can assume that the process of permanent (but reversible) single-shot NPs amorphization demands the well known steps for a general phase-change process of bulk GST material: (i) ultrafast heat absorption, (ii) overcoming of the melting temperature, (iii) fast quenching of the state via rapid heat dissipation through the substrate and embedding medium/capping layer. In particular, the spherical shape of the NPs maximizes the thermal contact with the external media, and the ultrafast quenching is ensured by a cooling rate on the order of 10^{10} K/s (estimated from $1/t_T$). In this respect, ablation occurs when the pump fluence is so high that the hot NPs, at $t > t_T$, release enough heat to ignite the whole PMMA volume above (at ~ 750 K). Therefore, the NPs are pull out from the substrate together with the capping layer.

An estimation of the heat actually absorbed by the nanoparticles is needed. The absorbance -defined as $A = -\log(T)$, where $T = I/I_0$ is the transmittance normalized with respect to the substrate- ranges from 0 (100% T) to 2 (1% T). We measured the absorbance (A) of crystalline GST NPs with diameter size 7.4 nm and 10.8 nm, normalized to the Mica substrate (see Fig. 18 a, main panel) in the visible (VIS) range 300 – 700 nm, using the spectrometer available at the BIO Lab (Elettra Synchrotron). In particular, absorbance at 400 nm (vertical dashed line) is equal to 0.25 and 0.26 for 7.8 nm and 10.8 nm NPs, respectively. In addition, inset of Fig. 18 a shows the absorbance of the 10.8 nm NPs in the near-infrared (n-IR) range 720 – 2400 nm, at the SISSI beamline (Elettra Synchrotron). Absorbance at 800 nm corresponds roughly to ~ 0.15 .

The maximum laser intensity absorbed is defined as $E_{abs} = E_{0,max} \times A'$, where A' is a slight over estimation of the absorption efficiency in percent (given by $1 - 10^{-A}$). The cross section σ of a single NP is approximated to the maximum value $\pi(d/2)^2$, for a sphere with diameter d . The energy absorbed ΔQ per NP is thus given by the

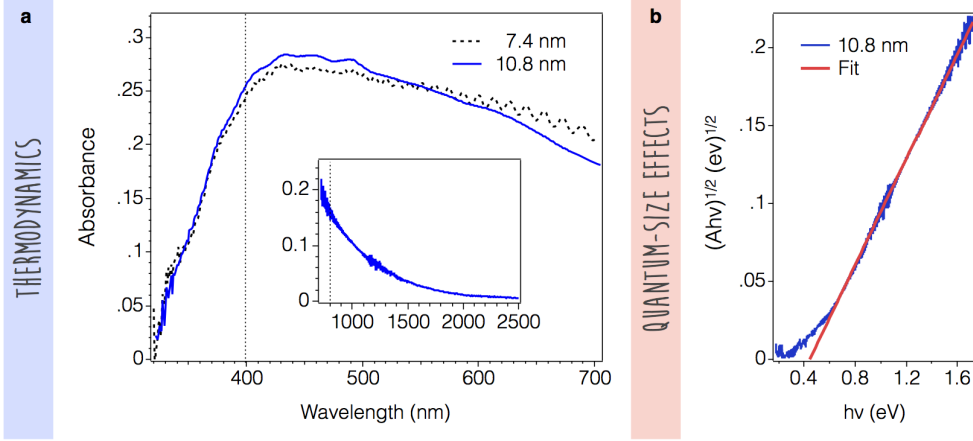


Figure 18: **a** Absorbance measured for crystalline GST NPs with diameter size 7.4 nm and 10.8 nm in the VIS (main) and n-IR (inset) energy ranges. **b** Tauc plot used for calculating the band gap of $\text{Ge}_2\text{Sb}_2\text{Te}_5$ NPs with 10.8 nm diameter.

product of E_{abs} and σ . Finally, by considering the tabulated specific heat c_p of the $\text{Ge}_2\text{Sb}_2\text{Te}_5$ [13], it is possible to relate the single laser pulse heat absorption to a determinate temperature increase, via the following thermodynamical relation:

$$\Delta Q = \rho V \int_{T_{RT}}^{T_{RT} + \Delta T_{\text{max}}} c_p(T) dT \quad (10)$$

where $\rho = 5.55 \times 10^4 \text{ mol/m}^3$ is the density of $\text{Ge}_2\text{Sb}_2\text{Te}_5$ (average between fcc and hex phases) and V is the volume of the spherical nanoparticle.

All the results of the fit and above calculations are reported in Table 4. According to the 30% NPs diameter reduction from 10.8 to 7.8 nm, a decrease of roughly 19% in the average threshold fluences (AM and ABL) is detected. The maximum temperature increase ΔT_{max} at the amorphizing threshold fluences is approximated to 510-550 K, one order of magnitude less than what obtained for ablation. These temperature values are estimated by assuming that the absorbed energy by electrons is fully transferred to the lattice within picoseconds, via electron-phonon coupling.[3] Other non-radiative relaxation pathways -like Auger recombination- may occur, decreasing the whole energy flow between the two subsystems. Although these effects would result in a lower ΔT_{max} of lattice, this correction is negligible to our

purposes. Therefore, since the measurements were taken at room temperature, the NPs T_{melt} is esteemed to be below the final temperature reached by the NPs: $T_{fin} = T_{RT} + \Delta T_{max} \sim 810 - 850$ K. This major decrease with respect to the 3-D counterpart value (890 K[14]), can be reported as a scaling effect. Indeed, compared to bulk, nano-scaled and strongly-confined materials have a higher surface-to-volume ratio, which consequently alters their thermal properties. As previously foreseen, a melting-point drop has been observed when the material's dimension decreases towards nanometer size.[15] For instance, the melting temperature of <5 nm GeTe thin films is 150 K below the bulk value[16], as well as GeTe nanowires, whose T_{melt} presents a 46% reduction.[17] Similarly, a T_{melt} depression has also been shown for metal[6; 18–20] and semiconductor[7; 21; 22] NPs. It is worth noting that, despite this temperature trend, the stability of the nano-materials amorphous phase is still preserved, as shown for GeTe nanoparticles by *Caldwell et al.*[21] This pioneering review outlines a positive preface for our $\text{Ge}_2\text{Sb}_2\text{Te}_5$ NPs case.

4.3.2 Quantum-Confinement Effects

Interestingly, possible *quantum-confinement* effects may occur in the electronic structure of our system of $\text{Ge}_2\text{Sb}_2\text{Te}_5$ NPs. The parameter defining the boundary between the bulk and the quantum confinement regimes is the Bohr Exciton Diameter[23]:

$$d_B = 2r_B \epsilon_{st} / (m^* / m_e) \quad (11)$$

where $r_B = 0.053$ nm is the Bohr Radius, ϵ_{st} is the static dielectric constant (electronic contribution), m^* is the effective mass and m_e is the bare electron mass. In the case of CdSe nano-crystals, a $\sim 15\%$ band gap increase is observed when dimensions are $d_B/2$. [23] The values for $\text{Ge}_2\text{Sb}_2\text{Te}_5$ ($\epsilon_{st} = 34.9$ [24], $(m^*/m_e) = 0.35$ [25]) give $d_B \sim 11$ nm. (A similar value was found for $\text{Ge}_1\text{Sb}_2\text{Te}_4$, i.e. 13 nm[26].) Therefore, since the NPs diameters ($d < 10.8$ nm) are on the same order of the Bohr exciton diameter, quantum confinement effects, like band gap increasing, can actually occur.

It is important to note that the energy gap in $\text{Ge}_2\text{Sb}_2\text{Te}_5$ is remarkably small (~ 0.38 eV[27; 28]). We considered the n-IR absorbance spectra (inset of Fig. 18 a) and to estimate the band gap in our system we used the Davis-Mott relations[27; 28]:

$$(Ah\nu)^{1/2} = C * (h\nu - E_g) \quad (12)$$

where $A = -\ln(T/T_{mica})$ is the measured absorbance, C is a constant including the thickness, h is the Plank's constant, ν is the frequency and E_g is the energy gap. Fig. 18 b displays the so-called Tauc-plot, where the intercept of the fit with the abscissa gives E_g . In this case, we found $E_g \sim 0.45$ eV, which is roughly 15% higher than that of bulk. Yet, this estimated band gap expansion does not affect the absorption process our system is involved in, due to the much higher pump energy ($\lambda = 400$ nm, 3.1 eV). In addition, in the low energy region, there is no evidence of other possible confinement effects, like plasmons.

4.3.3 Static Transmittivity

In order to benchmark the structure of the two NPs states, namely the “pristine”/crystalline state and the laser-treated state, we measured their difference in optical transmission at 800 nm (Fig. 19 a). The probe beam at 800 nm -being collinear with the pump and with a fluence below 0.06 mJ/cm²- was used to measure the transmission before and after the single-shot amorphization with $F_{\text{avg}} = 3$ mJ/cm². The relative difference in percent is presented as an histogram in Fig. 19 a. Each count is the average over 640 probe pulses with repetition rate of 1 kHz. The distribution has a mean value of $\sim 5\%$ and a standard deviation of 1 %.

Our aim is to give a comprehensive explanation of the reduced transmittivity contrast between the crystalline-amorphous NPs. In order to explain this transmittivity variation, we report both a comparison with thin film cases[29] and a theoretical simulation accounting for our system.

Nishiuchi et al.[29] measured the transmittivity in % at 633 nm during the phase transformation (from the amorphous to the crystalline state) via annealing of the following multilayer system:

- ZnS-SiO₂ (30 nm);
- Ge₂Sb₂Te₅ - various thickness;
- ZnS-SiO₂ (30 nm);
- Glass (0.3 mm) - substrate.

The values at 75° C and 280° C are representatives of the % transmission of the amorphous and crystalline states, respectively. The resulting transmittivity difference in % between the two states is shown in Fig. 20 a: around 10 nm is on the order of 10% and decreases further with decreasing thickness. The *tmm* python package[30] provides programs for calculating the light propagation (transmission, reflection) in multilayer thin films, considering multiple internal reflections and interferences -coherently or incoherently- via the *Transfer Matrix Method*. Therefore, we simulated the transmittivity data from *Nishiuchi et al.* with *tmm* python package, taking into account the nominal sample stacking and coherent interference. The simulations (dotted and dashed lines in Fig. 20 a) well resemble the data. Therefore, this method is reliable to account for transmittivity % calculations.

In 1904 J. C. Maxwell-Garnett developed a simple *effective medium theory* whereby the macroscopic properties of a composite material are derived.[31] In particular, it is possible to obtain the dielectric constant of spherical particles randomly dispersed in an insulator dielectric material. Briefly, the model averages the dielectric constants of the different materials (namely the external “matrix” and the particles), as long as the particles dimension is sufficiently large -for macroscopic Maxwell equations to be valid and obtain a frequency-dependent dielectric constant- but still small with respect to wavelength or attenuation length -for ensuring the dielectric constant of the whole

ensemble of particles.[32] The Clausius-Mossotti relation expresses a material's dielectric constant ϵ in terms of the polarizability of its constituent *particles*:

$$\left(\frac{\epsilon - 1}{\epsilon + 2}\right) = \frac{4\pi}{3} \sum_j \frac{n_j}{V} \alpha_j \quad (13)$$

where the sum is over different species/materials of the particles, n_j is the number of a species of particles, V is the total volume and α_j is the polarizability of a species of particles.

From electrostatics, the polarizability of a single species of particles i is given by:

$$\alpha_i = r^3 \left(\frac{\epsilon_i - 1}{\epsilon_i + 2}\right) \quad (14)$$

where ϵ_i is the species dielectric constant and r is the particles radius. By combining Eq. 13 and Eq. 14 and considering a general dielectric host material with ϵ_m , the Maxwell-Garnett equation is the following:

$$\left(\frac{\epsilon_{eff} - \epsilon_m}{\epsilon_{eff} + 2 * \epsilon_m}\right) = \rho_i \left(\frac{\epsilon_i - \epsilon_m}{\epsilon_i + 2 * \epsilon_m}\right) \quad (15)$$

where ϵ_{eff} is the effective dielectric constant of the particles embedded in the matrix and $\rho_i = (n_4\pi/3r^3)/V$, and this equation is solved by:

$$\epsilon_{eff} = \epsilon_m \left(\frac{\epsilon_i + 2\epsilon_m + 2\rho_i(\epsilon_i - \epsilon_m)}{\epsilon_i + 2\epsilon_m - \rho_i(\epsilon_i - \epsilon_m)}\right) \quad (16)$$

It is important to note that, although Maxwell-Garnett elaborated his theory considering only metal-included particles, the derivation is valid in general.[33]

For crystalline $\text{Ge}_2\text{Sb}_2\text{Te}_5$ the attenuation length at 800 nm is roughly 16.5 nm. Therefore, we could apply this theory and the above equations to our case of < 11 nm $\text{Ge}_2\text{Sb}_2\text{Te}_5$ crystalline nanoparticles embedded in a dielectric PMMA matrix and de-

termine the related “effective” dielectric constant. In particular, we used $\rho_i = 0.524$ corresponding to the thinnest regular packing, ϵ_m of PMMA and ϵ_i of $\text{Ge}_2\text{Sb}_2\text{Te}_5$, both at 800 nm.

Subsequently, we used the approach explained above with tmm python package to calculate the transmittivity at 800 nm of our multilayer system, which -in first approximation- can be consider to have the following stacking:

- PMMA (200 nm);
- monolayer-like deposited GST NPs embedded in PMMA matrix - various thickness;
- Mica (0.21 mm)- substrate.

The results as a function of the monolayer-like GST NPs thickness are shown in Fig. 20 b, for both coherent and incoherent interference. To account for possible NPs overlap (see Section 4.2), a layer thickness between 1 and 3 times the NPs diameter -i.e. 10-30 nm- has to be considered. The *absolute transmittivity in %* for the crystalline state corresponds to 67-77 % (blue box). From the measured absorbance A at 800 nm for crystalline 10.8 nm NPs (see inset of Fig. 18a), it is possible to obtain the absolute transmittivity from:

$$T = 10^{-A} = 10^{-0.15} \sim 71\% \quad (17)$$

This value resides in the range of the simulated transmittivity, in both coherent and incoherent cases.

The grey box highlights the *transmittivity difference in %* in the 10-30 nm layer thickness range that correspond to an interval between 2-10 %. Again, the measured transmittivity difference of 5(1) % (see Fig. 21) lies within this range. Despite successfully modelling the optical properties of such complex systems is still a great challenge, joining the Maxwell-Garnett approximation theory to the computation power of the tmm package tool led to excellent agreement between experimental data and simulations of $\text{Ge}_2\text{Sb}_2\text{Te}_5$ nanoparticles transmittivity.

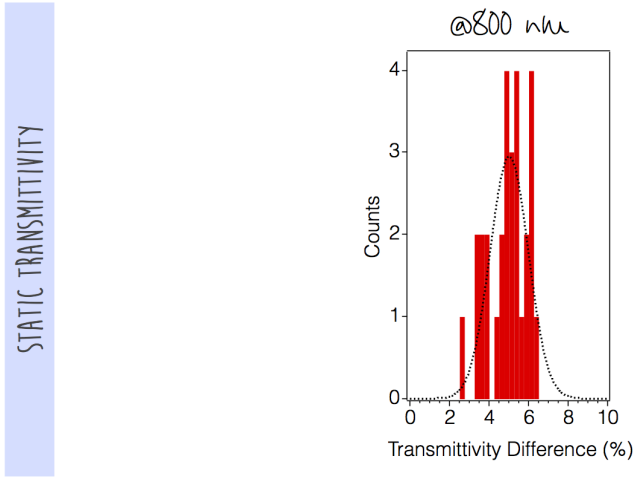


Figure 19: Transmittivity difference, before and after single shot amorphization, measured with a 800 nm laser probe at 1 kHz repetition rate.

4.3.4 X-Ray Diffraction

XRD measurements were performed to demonstrate that a structural difference between the unaltered and laser-treated NPs occurs. Hence, we optically prepared an homogeneous single-shot amorphized square area of $1 \times 1 \text{ mm}^2$ on the 10.8 nm NPs sample, by using a pump average fluence of 3 mJ/cm^2 . RD measurements were performed at the XRD1 beamline in the Elettra Synchrotron facility. The photon energy was 12.4 keV -resonant to the Ge K-edge- and the beam size at the sample was focussed to $500 \times 200 \text{ }\mu\text{m}^2$. XRD radial patterns were acquired in transmission mode with a Dectris Pilatus 2M detector with an exposure time of 600 s on: (i) unaltered, (ii) laser-amorphized and (iii) pure substrate regions. Fig. 21 a shows a complete XRD image, where the main signal (high intensity spots) comes from the diffraction peaks of the crystalline Mica substrate while the crystalline NPs contribution is visible as a weak “ring-like” signal (the white dotted line is a guide-to-the-eye). Nonetheless, by radial-integrating the images, it was possible to isolate this low NPs contribution. The peak at 17.9° can be ascribed to the (103) diffraction plane of the hexagonal lattice with $a = 0.434(5) \text{ nm}$ and $c = 1.864(5) \text{ nm}$. In addition, by applying the Scherrer's equation[34] with the extracted line broadening of the peak -out of the instrumental one- the resulting “grain”-size is $9.7(9) \text{ nm}$, which is compatible with our NPs size. Fig.

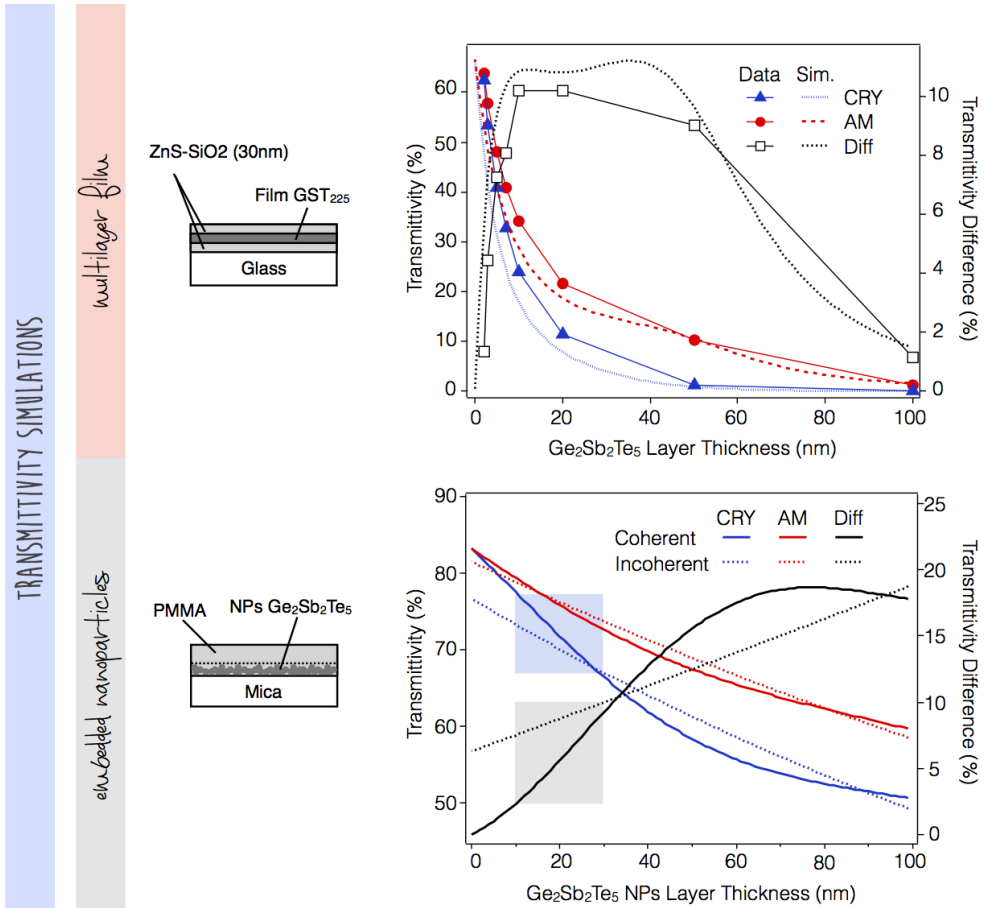


Figure 20: **a** Experimental and simulated transmittivity and AM-CRY transmittivity difference of a GST thin film with various thickness (from *Nishiuchi et al.*[29]). **b** Simulated transmittivity and AM-CRY transmittivity difference of a monolayer-like deposited GST NPs embedded in PMMA matrix with different thickness.

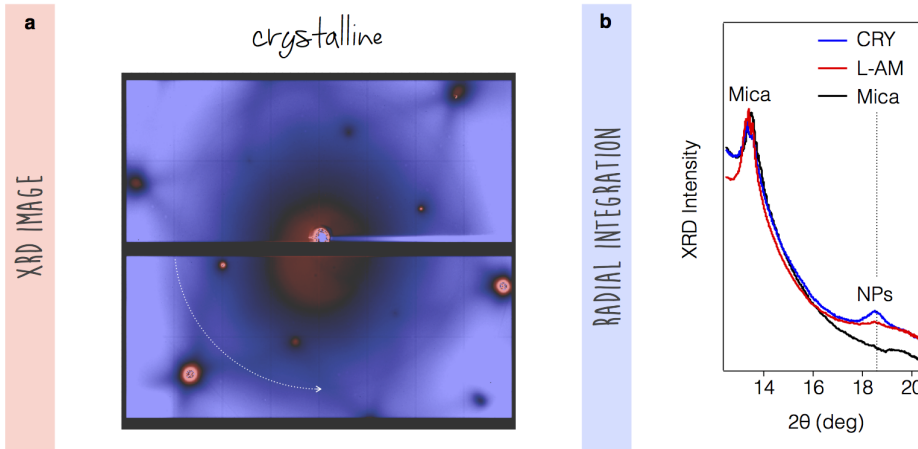


Figure 21: **a** XRD image of crystalline $\text{Ge}_2\text{Sb}_2\text{Te}_5$ NPs. The white dashed curved line is a “guide-to-the-eye” for the very low intensity signal coming from the crystalline NPs. This annular signal is typical of powder-like samples. **b** XRD radial integrated profiles in the 2θ angular range corresponding to the diffraction peak of the GST nanoparticles. This peak is highly suppressed in the laser-amorphized sample.

21 b displays the XRD intensity for the three regions probed as a function of 2θ angle, in the range where the diffraction peak of the GST NPs appears. The peak is visible in the crystalline zone, is reduced and broader in the laser excited region and is absent in the substrate. This qualitative observation is consistent with our assumption of NPs single-shot optical amorphization.

4.3.5 Comparison with Thin Films

The remarkable low critical amorphization fluence of GST NPs deviates considerably from the corresponding values found for higher dimensional GST systems. Fig. 22 presents a comparison between critical fluences of femtoseconds single-shot amorphization for $\text{Ge}_2\text{Sb}_2\text{Te}_5$ thin films with various thicknesses [1–4] and the case of study. For a laser wavelength of 800 nm, it is possible to observe a decreasing trend of critical level fluence as the film thickness is reduced. It has also been demonstrated that the use of the laser second harmonic (400 nm) lowers the critical level roughly of 20% [5]. Consistently, we calculated the expected 10.8 nm NPs amorphization fluence for a 800 nm pump pulse. The corresponding absorbance (inset of Fig. 18 a) converted

Amorphization

| d [nm] | σ [$\times 10^{-13}$ cm ²] | A' | F_{avg} [mJ/cm ²] | $E_{0,max}$ [mJ/cm ²] | ΔQ_{max} [$\times 10^{-16}$ J] | ΔT_{max} [K] |
|------------------|---|-----------|------------------------------------|--------------------------------------|--|-------------------------|
| 7.4 | 3.3(2) | 0.43 | 0.52(5) | 1.0(1) | 1.9(2) | 550(50) |
| 10.8 | 7.2(6) | 0.45 | 0.64(7) | 1.3(2) | 5.4(5) | 510(50) |

Ablation

| d [nm] | σ [$\times 10^{-13}$ cm ²] | A' | F_{avg} [mJ/cm ²] | $E_{0,max}$ [mJ/cm ²] | ΔQ_{max} [$\times 10^{-16}$ J] | ΔT_{max} [K] |
|------------------|---|-----------|------------------------------------|--------------------------------------|--|-------------------------|
| 7.4 | 3.3(2) | 0.43 | 6.9(6) | 13(1) | 2.6(3) | ~ 7000 |
| 10.8 | 7.2(6) | 0.45 | 7.2(7) | 14(1) | 5.9(6) | > 6000 |

Table 4: Absorbance and cross-section parameters of Ge₂Sb₂Te₅ nanoparticles. The average threshold fluence (F_{avg}) and the laser peak maximum energy density ($E_{0,max}$) -for both amorphization and ablation processes- are used to calculate the maximum heat absorbed and temperature increase of the nanoparticles. Errors are presented in parentheses

in percent is $A'(800 \text{ nm}) = 0.29$, and the peak power threshold is then approximately 2 mJ/cm². In contrast to similar thickness thin films, the NPs critical energy density is 4 times smaller. In the case of a 400 nm exciting pump, the fluence is further reduced to a total factor 7. As mentioned in the introduction, these reduction factors account for the decrease of the melting temperature, optimal choices of substrate and capping layer materials and ideal cooling conditions for NPs. As shown in the close-up inset of Fig. 22, the critical fluences for the two sizes NPs differ of about 19 % and a consistent trend can be likely foreseen also for smaller or bigger NPs. Yet, at this stage, growth conditions and different optical response defines our careful dimensional strategy, which proved to be highly efficient in demonstrating the advantages of NPs over thin films. Indeed, when going from a continuous thin film to a (porous) film containing discrete nano-sized particles, the energy required for amorphization is highly reduced, which is a very relevant result from the application point of view.

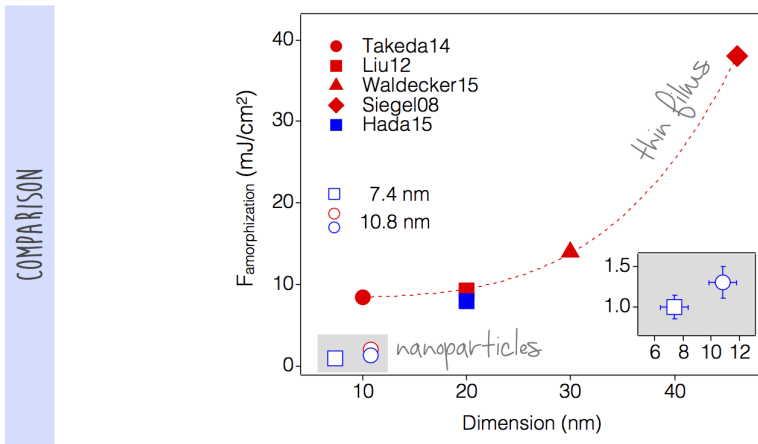


Figure 22: Comparison between average threshold fluences for ultrafast single shot amorphization, with 800 nm (red marks) or 400 nm (blue marks) laser pulses, on thin films (filled marks) and nanoparticles (empty marks) as a function of thickness or dimension. Inset shows a close-up of the nanoparticles data, highlighting the difference between the two diameter sizes.

4.4 CONCLUSIONS

Laser-induced single-shot amorphization has proved successful in phase-change materials thin films.[1–5] Here we demonstrated a dimensional reduction strategy to dramatically enhance the energy efficiency of the optical amorphisation of 0-dimensional $\text{Ge}_2\text{Sb}_2\text{Te}_5$. Accordingly, the dimensional scalability of the phase-change mechanism in GST NPs is also confirmed. With single-shot ultrashort laser pulses at 400 nm, we amorphized nanometer-size $\text{Ge}_2\text{Sb}_2\text{Te}_5$ particles deposited on Mica substrate and capped with a PMMA layer. Reversibility without damage is the basic requirement for a successful operating memory device. Noteworthy, we found an average fluence *working-range* between 0.6–6 mJ/cm^2 where NPs can be amorphized without being destroyed or removed from the substrate. The location of this excitation energy-window ($< 10 \text{ mJ}/\text{cm}^2$) along with its competitive relative extension (90% instead of 70% for $\text{Ge}_2\text{Sb}_2\text{Te}_5$ 10 nm thin film[1]) will lead to superior implementation of NPs in industrial devices. Based on our findings, we can also envisage the technologically relevant single nanoparticle phase switching with an arbitrary laser pulse size, as long as the energy fluence at the pulse center exceeds the amorphization limit (i.e.

$\sim 1 \text{ mJ/cm}^2$). The enhancement on the RESET process shown in this work, involving a melting temperature reduction, is strictly and positively connected to the improvement on the SET process, where a minor size-dependent increase in the crystallization temperature (422–428 K) was observed in similar system by *Chen et al.*[8] Also the repeated cycles of single-shot and annealing treatments -performed in this work- confirm the constant value of the crystallization temperature at 425 K. Indeed, the resulting operation window simultaneously allows a low power consumption and a high crystallization rate. In addition, the stability of the amorphous phase was ensured by growth condition via adding methane and was also observed experimentally, since the laser marks will permanently last if no annealing is performed. All these aspects are of paramount relevance concerning the progress of future technologies design and production on the nanoscale limit. Finally, our work is an example demonstrating the benefit of taking advantage of scalable GST properties to optimally control the crystal-to-amorphous switching mechanism.

BIBLIOGRAPHY

- [1] J. Takeda, W. Oba, Y. Minami, T. Saiki, and I. Katayama. *Applied Physics Letters*, 104(26):261903, 2014.
- [2] Y. Liu, M. M. Aziz, A. Shalini, C. D. Wright, and R. J. Hicken. *Journal of Applied Physics*, 112(12):123526, 2012.
- [3] L. Waldecker, T. A. Miller, M. Rude, et al. *Nature Materials*, 14(10):991–995, 2015.
- [4] J. Siegel, W. Gawelda, D. Puerto, et al. *Journal of Applied Physics*, 103(2):023516, 2008.
- [5] M. Hada, W. Oba, M. Kuwahara, et al. *Scientific Reports*, 5:13530 EP –, 2015.
- [6] P. Buffat and J.-P. Borel. *Physical Review A*, 13:2287–2298, 1976.
- [7] H. H. Farrell and C. D. V. Siclen. *Journal of Vacuum Science & Technology B: Microelectronics and Nanometer Structures Processing, Measurement, and Phenomena*, 25(4):1441–1447, 2007.
- [8] B. Chen, G. H. ten Brink, G. Palasantzas, and B. J. Kooi. *Scientific Reports*, 6:39546, 2016.
- [9] J. M. Liu. *Optics Letters*, 7(5):196–198, 1982.
- [10] V. K. Pustovalov. *Chemical Physics*, 308(1):103 – 108, 2005.
- [11] B. B. Kadhim, F. K. Farhan, B. D. Balwa, and W. A. Shakir. *Science and Technology*, 7(1):1–3, 2017.
- [12] T. P. Inc. Properties and chemical composition of mica grade v1, grade classification of muscovite mica, 2017. URL https://www.tedpella.com/Vacuum.html/Mica_Grade_V1_Properties.html.
- [13] P. Zalden, K. S. Siegert, S. Rols, et al. *Chemistry of Materials*, 26(7):2307–2312, 2014.
- [14] N. Yamada, E. Ohno, K. Nishiuchi, N. Akahira, and M. Takao. *Journal of Applied Physics*, 69(5):2849–2856, 1991.
- [15] Y. F. Zhu, J. S. Lian, and Q. Jiang. *The Journal of Physical Chemistry C*, 113(39):16896–16900, 2009.
- [16] S. Raoux, R. M. Shelby, J. Jordan-Sweet, et al. *Microelectronic Engineering*, 85(12):2330 – 2333, 2008.

- [17] X. Sun, B. Yu, G. Ng, and M. Meyyappan. *The Journal of Physical Chemistry C*, 111(6):2421–2425, 2007.
- [18] G. Allen, R. Bayles, W. Gile, and W. Jesser. *Thin Solid Films*, 144(2):297 – 308, 1986.
- [19] S. L. Lai, J. Y. Guo, V. Petrova, G. Ramanath, and L. H. Allen. *Physical Review Letters*, 77:99–102, 1996.
- [20] J. Sun and S. Simon. *Thermochimica Acta*, 463(1):32 – 40, 2007.
- [21] M. A. Caldwell, S. Raoux, R. Y. Wang, H.-S. Philip Wong, and D. J. Milliron. *J. Mater. Chem.*, 20:1285–1291, 2010.
- [22] Z. Liu, X. Sui, K. Kang, and S. Qin. *The Journal of Physical Chemistry C*, 119(21):11929–11933, 2015.
- [23] A. M. Smith and S. Nie. *Accounts of Chemical Research*, 43(2):190–200, 2010.
- [24] E. Prokhorov, J. J. Gervacio-Arciniega, G. Luna-Bárcenas, et al. *Journal of Applied Physics*, 113(11):113705, 2013.
- [25] J. Kellner, G. Bihlmayer, M. Liebmann, et al. *Communications Physics*, 1(1):5, 2018.
- [26] T. Siegrist, P. Jost, H. Volker, et al. *Nature Materials*, 10(3):202–208, 2011.
- [27] E. Vinod, R. Naik, R. Ganesan, and K. Sangunni. *Journal of Non-Crystalline Solids*, 358(21):2927 – 2930, 2012.
- [28] E. M. Vinod, K. Ramesh, and K. S. Sangunni. *Scientific Reports*, 5:8050, 2015.
- [29] K. Nishiuchi, N. Yamada, K. Kawahara, and R. Kojima. *Japanese Journal of Applied Physics*, 46(11R):7421, 2007.
- [30] S. J. Byrnes. *arXiv preprint arXiv:1603.02720*, 2016.
- [31] J. C. Maxwell Garnett. *Philosophical Transactions of the Royal Society of London A: Mathematical, Physical and Engineering Sciences*, 203(359-371):385–420, 1904.
- [32] R. W. Cohen, G. D. Cody, M. D. Coutts, and B. Abeles. *Physical Review B*, 8: 3689–3701, 1973.
- [33] R. J. Gehr and R. W. Boyd. *Chemistry of Materials*, 8(8):1807–1819, 1996.
- [34] A. L. Patterson. *Physical Review*, 56:978–982, 1939.

5

TIME-RESOLVED TRANSMITTIVITY OF GST NANOPARTICLES

ABSTRACT

Previously we demonstrated the optical amorphization of $\text{Ge}_2\text{Sb}_2\text{Te}_5$ nanoparticles by using single pulses at 400 nm of $\sim 0.6\text{--}0.8\text{ mJ/cm}^2$ average fluence. This Chapter aims at revealing the ultrafast time-resolved scenario of the optical properties of crystalline $\text{Ge}_2\text{Sb}_2\text{Te}_5$ 10.8 nm NPs below the phase transformation threshold fluence. In particular, transmittivity pump-probe measurements will be presented in details. The rapid optical change will be linked to a sudden de-population of electronic resonant bonding states. Furthermore, coherent optical phonons emerge in the resulting metastable/transient state living for few ps.

5.1 INTRODUCTION

In **equilibrium** conditions, the two phases of GST materials present sharp differences in electrical, optical and structural properties, which are strongly coupled together (see Chapter 1 for details). In particular, GST alloys are average V-valent materials with five valence *sp*-electrons[1], where the large energy difference between s- and p-electronic levels inhibits the hybridization. Hence, only the p-electrons play a key role in the chemical bond formation. Along a single axis, just one electron is available for the two nearest neighbours, giving rise to two energetically degenerate configurations, which can superimpose to establish a new lower ground state. This long-range bonding is called “resonant”.[2; 3] Atomic distortions (as Peierls-like) -favoring one of the two configurations- can counteract the resonance effect, which eventually dominates for small displacements.[4] The large contrast in the dielectric constant is ascribed to the resonant bonding, which, in turns, becomes one of the main fingerprints of the crystalline phase with respect to the amorphous phase, where long- or medium-range alignment of the *p*-orbitals is absent.[5] However, it is worth noting that the differences in the dielectric constants have been also explained by simple semiconductor arguments, considering a distinct -on average- band gap of amorphous and crystalline structures, without resonant bonding.[6–8]. Therefore, up to now, there is still no common agreement on the dominance of resonant bonds in the structure and thus in the optical properties, of phase change materials. “Indirect” experiments -like IR reflectivity and ellipsometry spectroscopy[9]- along with DFT and ab initio calculations of the dielectric constant of crystalline phase-change materials[10] have been performed in order to demonstrate the existence and relevance of this phenomenon. Yet, to our knowledge a proper understanding of this issue is still missing.

In **out-of-equilibrium** conditions, the connection between optical response and structural transition is weaker. It has been shown that ultrafast photoexcitation, with low fluence, produces a large change in the optical properties of a GST thin film in a much shorter time-scale with respect to the structural permanent amorphization.[11] The Authors associated the resulting transient state to a complete removal of the resonant bonding and is a current valid interpretation. Rapid optical control without

structural changes leads to higher switching speed and less power consumption, even though losing non-volatility. This result pioneers alternative perspectives for GST as being integrated in optical modulators or other photonic devices.

Therefore, in this section, we will present the optical transmittivity change of crystalline GST NPs following the excitation with femtosecond laser pulses *without* inducing structural amorphization. The aim of these measurements is to understand if and how the dynamics in a spatial confined GST material can give more information on the fundamental bond nature.

5.2 EXPERIMENTAL RESULTS

We considered the sample of $\text{Ge}_2\text{Sb}_2\text{Te}_5$ nanoparticles, with diameter 10.8 nm, deposited on Mica and capped with PMMA. The optical setup used is the one described in Chapter 2 Section 2.2. The probe wavelength was 800 nm with an average fluence of 0.06 mJ/cm^2 . The pump wavelength was 400 nm with an average fluence of 0.15 mJ/cm^2 , much lower than the threshold fluence for permanent amorphization ($\sim 0.6 \text{ mJ/cm}^2$).

The measurements were performed at a 1 kHz repetition rate, since the surface-to-volume ratio of the NPs ensures the complete recovery of the sample -in terms of thermal dissipation/accumulation- between subsequent laser pulses. Thus, no visible changes in the sample were observed during the measuring session, for the fluences and repetition rate reported here.

Fig. 23 (black lines) shows the time-resolved changes in transmittivity (T) of GST NPs. We have seen that -by considering from the absorbance at 800 nm- the absolute static transmittivity of our crystalline GST 10.8 nm NPs is on the order of 70 % (see Chapter 4, Section 4.3.3). Here, at short time-scales up to few ps, a prompt but small decrease in transmission ($\sim 10^{-3} \%$) with a weak oscillatory modulation occurs. In order to investigate and interpret this dynamics, we decided to follow two complementary approaches: (i) theoretical data-simulation and (ii) data-fitting.

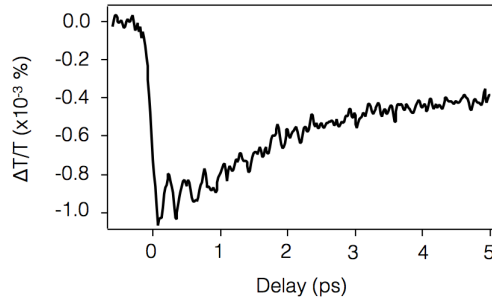


Figure 23: Experimental pump(400 nm)-probe(800 nm) data acquired on $\text{Ge}_2\text{Sb}_2\text{Te}_5$ nanoparticles. The pump fluence was 0.15 mJ/cm^2 .

5.2.1 Data Simulation

A theoretical simulation of a material's **out-of-equilibrium** transmittivity (or reflectivity) requires the knowledge of the **out-of-equilibrium** behaviour of a fundamental property, like the complex dielectric constant.

Waldecker et al.[11] performed pump-probe (800 nm-800 nm) simultaneous transmittivity and reflectivity measurements on a 30 nm thin film of $\text{Ge}_2\text{Sb}_2\text{Te}_5$, with variable pump fluence up to 6 mJ/cm^2 . From these data they extracted the ϵ_1 and ϵ_2 dynamics by the transfer matrix method. It is important to note that these extracted behaviours are fundamental properties of the material itself, regardless of the dimensions (3-D, 2-D, 1-D or 0-D). The same authors also found that the threshold fluence for amorphization of this system was 14 mJ/cm^2 .

In our case, we found that the threshold pump fluence at maximum for amorphization of the 10.8 nm NPs system was 1.3 mJ/cm^2 . We performed time-resolved measurements at 0.15 mJ/cm^2 pump fluence, which is the 12 % of the threshold pump fluence at maximum. The $\text{Ge}_2\text{Sb}_2\text{Te}_5$ ϵ_1 and ϵ_2 dynamics in *Waldecker et al.*[11] scales linearly with fluence. To obtain a dynamics with a 12 % of pump threshold fluence -i.e. 1.68 mJ/cm^2 - we considered the one taken at 2 mJ/cm^2 pump fluence (dark green line in Ref. [11]) multiplied by 0.84. Fig. 24 left panel shows the $\text{Ge}_2\text{Sb}_2\text{Te}_5$ dielectric constant dynamics (real and imaginary parts) considered in our simulation. Starting from these data, we computed the “effective” dielectric constant as a func-

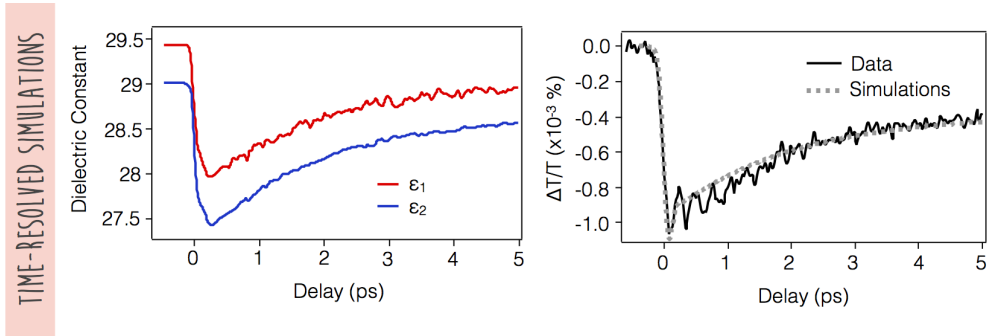


Figure 24: **Left panel:** Real (ϵ_1) and imaginary (ϵ_2) part of the dielectric function as a function of time, corresponding to a pump fluence of 1.68 mJ/cm^2 . Reproduced from Ref. [11]. **Right panel:** experimental pump-probe data with superimposed pump-probe simulated data using the Maxwell-Garnett “effective” medium theory[13] and tmm python package[12] for calculating the transmittivity of a multilayer system.

tion of time of $\text{Ge}_2\text{Sb}_2\text{Te}_5$ nanoparticles randomly dispersed in a dielectric medium (PMMA) using the Maxwell-Garnett theory, described in Section 4.3.3, with thinnest regular packing ($\rho_j = 0.524$). Subsequently, using the python programs in the tmm package[12] we simulated the transmittivity at 800 nm as a function of time of our multilayer system:

- PMMA (200 nm);
- monolayer-like deposited GST NPs embedded in PMMA matrix - (30 nm)
- Mica (0.21 mm)- substrate.

Fig. 24 right panel - dashed black line shows the transmittivity dynamics for multilayer incoherent interference. It is possible to note that the simulation well resemble the experimental data. Hence, anew, the Maxwell-Garnett approximation theory proved successful in theoretically modelling the optical properties of nanoscale composite materials, in particular of $\text{Ge}_2\text{Sb}_2\text{Te}_5$ spherical nanoparticles deposited onto an optically transparent substrate and dispersed in a dielectric medium. This result foresees the possibility to use a very simple approach for reproducing the optical response of highly-complex systems and get a reliable and reproducible first-order approximation.

5.2.2 Fitting Procedure

The nanoparticles transmittivity dynamics $\Delta T/T(\%)$ has been reconstructed by considering a phenomenological model, in order to extract the amplitudes and time-scales of the processes involved. In particular we used a fitting function given by these three terms:

1. Gaussian Function (models the pump pulse):

$$g(t) = \frac{1}{\sqrt{2\pi}\sigma} e^{-\frac{(t-t_0)^2}{2\sigma^2}} \quad (18)$$

where σ is the standard deviation and t_0 is the coincidence time between pump and probe;

2. Step Function (represents the arrival of the pump pulse):

$$\theta(t - t_0) \quad (19)$$

3. Exponential Functions (expresses the recovery):

$$f(t) = Ae^{-\frac{(t-t_0)}{\tau}} + B(1 - e^{-\frac{(t-t_0)}{\tau}}) \quad (20)$$

where τ is the recovery time of the optical signal.

Firstly, Eq. 19 and 20 are combined in a product:

$$h(t) = \theta(t - t_0) \cdot f(t) \quad (21)$$

which is then convolved with Eq. 18 - accounting for the experimental resolution:

$$H(t) = (h \otimes g)(t) = \int_{-\infty}^{+\infty} h(\tau)g(t-\tau)d\tau \quad (22)$$

In our case, t_0 was fixed to 0 fs. Fig. 25 left panel shows the different contributions to the fitting function, while Fig. 25 right panel displays the result of the fitting proce-

| Fitting Parameters | |
|--------------------|---------------|
| A (%) | -1.011(8) E-3 |
| B (%) | -0.295(7) E-3 |
| τ (ps) | 2.20(7) |
| σ (fs) | 58(3) |

Table 5

ture with an excellent agreement with experimental data. The resulting fit parameters are displayed in Tab. 5.

5.3 DISCUSSION

A 400 nm (3.15 eV) optical excitation of $\text{Ge}_2\text{Sb}_2\text{Te}_5$ -whose band gap is $\sim 0.4\text{--}0.5$ eV- promotes electrons from the occupied-valence states to the unoccupied-conduction states, following holes creation.

In general, this results in a large free-carrier density which affects the dielectric functions by means of free-carrier absorption (i.e. Drude contributions), within the first hundreds of femtoseconds. In particular, ϵ_1 decreases while ϵ_2 increases.[14] On the contrary, according to our simulation results, we can ascribe the drop in NPs transmittivity to a large decrease in both real and imaginary part of ϵ (see Fig. 24). Hence, the observed response cannot only be described by free-carrier effects.

Since the loss of resonant bonding yields a reduction of ϵ_1 and ϵ_2 , *Waldecker et al.* suggested that, during photo-excitation, the incoming photons deplete the carriers (electrons) in the resonant bond states (i.e. via photobleaching).[11] This process at roughly ~ 100 fs induces a *transient out-of-equilibrium state* of $\text{Ge}_2\text{Sb}_2\text{Te}_5$ which lasts until lattice heating/thermalization occurs in ~ 2 ps. Fig. 26 illustrates a schematic diagram of the subsequent steps $\text{Ge}_2\text{Sb}_2\text{Te}_5$ is involved in, during and right after photo-excitation.

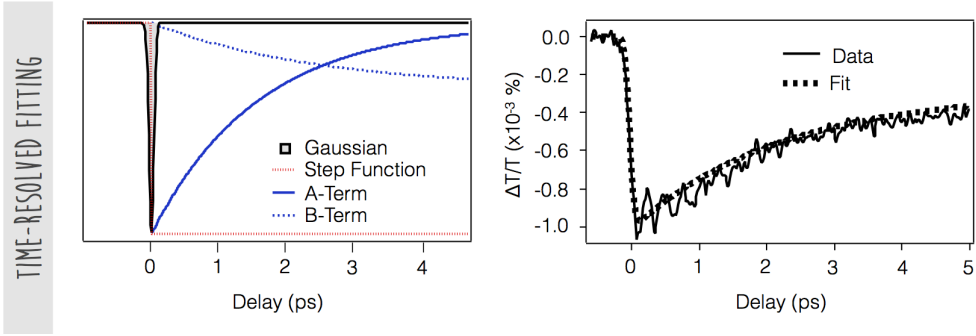


Figure 25: **Left Panel:** Individual terms that appear in the phenomenological fit function (Eq. 18, 19, 20). **Right Panel:** Experimental pump-probe data with superimposed fit result.

In first approximation, we can describe the dynamics of $\text{Ge}_2\text{Sb}_2\text{Te}_5$ nanoparticles analogously but other possible interpretations could be valid. In particular, according to the fitting procedure results, we unveiled a 2.2 ps recovery time (τ) for 0.15 mJ/cm^2 excitation fluence which regards the equilibration between excited carriers and lattice. In this context, we attributed the $-Ae^{-(t-t_0)/\tau}$ term to the dynamics of the resonant bond states. Remarkably, this time constant is higher than the $\sim 1.78 \text{ ps}$ -short time scale- found for the comparable fluence of $\sim 1.68 \text{ mJ/cm}^2$ in the case of thin films.[11] Indeed, the dimensionality confinement to 0-D delays the reformation of resonant bonding. Photo-excitation suppresses the majority of resonant bonds in a single nanoparticle. The “isolation” of nanoparticles between each other prevents from replicating the same bonding of unperturbed nanoparticles, re-establishing the resonant bonds. Therefore, the transient states lives a little longer in nanoparticles with respect to thin films. However, from a technological point of view, this difference in recovery time has no particular meaning.

Interestingly, we also observed oscillations in the time window up to 2 ps (see Fig. 23). Therefore, after the fitting procedure, we extracted the residuals, plotted in Fig. 27a. A Fourier Transform was performed in order to determine accurately the oscillation frequency, which resulted to be about 3.7(3) THz. As shown in Fig. 27b, this frequency agrees with the static Raman spectrum of crystalline $\text{Ge}_2\text{Sb}_2\text{Te}_5$. Here is shown an example of experimental Raman data by *De Bastiani et al.*[15], but these

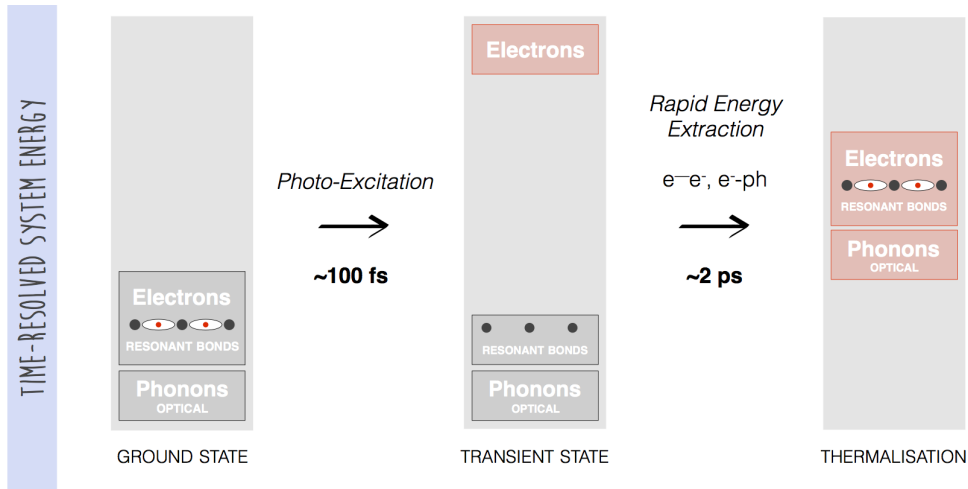


Figure 26: Schematic representation of the steps during ultrafast optical measurements. $\text{Ge}_2\text{Sb}_2\text{Te}_5$ in the ground state presents covalent and resonant bonding, defining its optical properties. Upon photo-excitation the resonant bonding states are depleted, producing a transient state at roughly ~ 100 fs. If there is a rapid release of energy, after ~ 2 ps the total system thermalize. Adapted from Ref. [5; 11]

spectra are consistent with other measurements[5; 16] and calculations[17] present in literature.

Ge-Sb-Te alloy systems are based upon the combination of binary GeTe and Sb_2Te_3 compounds. Therefore, it is possible to assume that the coherent phonon spectrum of GST keeps trace of its components phonon spectra. In β -GeTe (NaCl-type) only an IR-active mode exist at 2.94 THz[18], while Sb_2Te_3 presents a dominating degenerate E_g mode at 3.6 THz.[19; 20] $\text{Ge}_2\text{Sb}_2\text{Te}_5$ crystallized at $\sim 150 - 160^\circ$ C has a NaCl-type lattice structure, where one site is occupied by Te atoms and the other by Ge/Sb atoms or vacancies. The broad Raman spectrum of crystalline $\text{Ge}_2\text{Sb}_2\text{Te}_5$ towards lower frequencies (Fig. 27b) is due to the presence of random vacancies in the lattice, leading to bond-length increase and consequent force-constant spread, regulating the phonon modes.[17] The Raman-active coherent optical phonons observed in our measurements are due to local atomic motion near vacancies[5] and resemble the layers *in-plane* (111) vibration occurring in Sb_2Te_3 .

In addition, recently the transient state induced by optical excitation -where a sudden

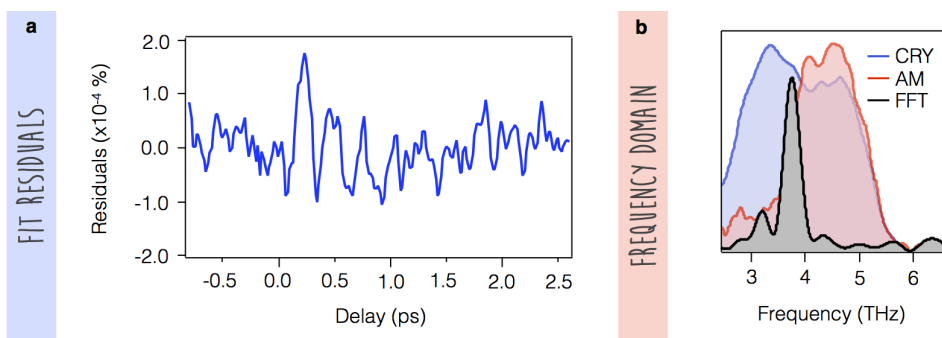


Figure 27: **a** Residuals extracted from the experimental data after the fitting procedure. An oscillation is clearly visible within the first picosecond after the pump arrival. **b** Static Raman measurements performed by *De Bastiani et al.*[15] for crystalline (blue solid line) and amorphous (red solid line) $\text{Ge}_2\text{Sb}_2\text{Te}_5$ thin films. An increased weight at low frequencies is visible for the crystalline phase. The black solid line corresponds to the Fourier Transform of the residuals, with a central peak at about 3.7 THz which agrees well with the static Raman measurements for the crystalline phase.

loss of resonant bonding occurs- is characterized by a so-called “rattling motion” of Ge (or Te) atoms. Briefly, these atoms move around their equilibrium-center position thus breaking the p -orbital alignment.[21]

5.4 CONCLUSIONS

In summary, in this chapter we have shown the first optical pump-probe (400 nm-800 nm) measurements taken on $\text{Ge}_2\text{Sb}_2\text{Te}_5$ < 11 nm nanoparticles. We detected a drop in transmittivity as slight as of $\sim 0.001\%$. Initially, we deeply investigated these time-resolved data through a theoretical simulation. It was found that the decreasing dynamics of both ϵ_1 and ϵ_2 of $\text{Ge}_2\text{Sb}_2\text{Te}_5$ joined to the Maxwell-Garnett theory can properly model the nanoparticles dynamics. This suggested the presence of a photo-induced transient state living for few ps, where possibly resonant bonding -typical of $\text{Ge}_2\text{Sb}_2\text{Te}_5$ crystalline material- is completely suppressed and structural changes not yet occur. According to this picture, it is important to note that the extension of the resonant bonding is below the dimensions of a single nanoparticle (<11 nm), leading to a limited range order. In addition, through a fitting process we found a recovery

time of ~ 2.2 ps. Finally, optical Raman-active phonons at ~ 3.7 THz characterizes the few ps dynamics after excitation, yielding Ge/Te atoms vibrations around their central position.

Hence, the possibility of selectively breaking the resonant bonds with very low optical fluence in 0-D $\text{Ge}_2\text{Sb}_2\text{Te}_5$, giving rise to a bit longer-lived transient state with respect to 2-D systems, pioneers new concepts of memory device functioning for storing and processing of data.

BIBLIOGRAPHY

- [1] J.-J. Kim, K. Kobayashi, E. Ikenaga, et al. *Physical Review B*, 76:115124, 2007.
- [2] L. Pauling. *The Nature of the Chemical Bond*. Cornell University Press, Ithaca, NY, 1939.
- [3] G. Lucovsky and R. M. White. *Physical Review B*, 8:660–667, 1973.
- [4] D. Lencer, M. Salinga, and M. Wuttig. *Advanced Materials*, 23(18):2030–2058, 2011.
- [5] T. A. Miller, M. Rudé, V. Pruneri, and S. Wall. *Physical Review B*, 94:024301, 2016.
- [6] K. Shimakawa, L. Střížik, T. Wagner, and M. Frumar. *APL Materials*, 3(4):041801, 2015.
- [7] R. O. Jones. *Journal of Physics: Condensed Matter*, 30(15):153001, 2018.
- [8] R. Yokota. *Japanese Journal of Applied Physics*, 28(8R):1407, 1989.
- [9] K. Shportko, S. Kremers, M. Woda, et al. *Nature Materials*, 7(8):653–658, 2008.
- [10] B. Huang and J. Robertson. *Physical Review B*, 81:081204, 2010.
- [11] L. Waldecker, T. A. Miller, M. Rude, et al. *Nature Materials*, 14(10):991–995, 2015.
- [12] S. J. Byrnes. *arXiv preprint arXiv:1603.02720*, 2016.
- [13] J. C. Maxwell Garnett. *Philosophical Transactions of the Royal Society of London A: Mathematical, Physical and Engineering Sciences*, 203(359-371):385–420, 1904.
- [14] L. Huang, J. P. Callan, E. N. Glezer, and E. Mazur. *Physical Review Letters*, 80:185–188, 1998.
- [15] R. De Bastiani, A. M. Piro, M. G. Grimaldi, et al. *Applied Physics Letters*, 92(24):241925, 2008.
- [16] P. Nemeč, A. Moreac, V. Nazabal, et al. *Journal of Applied Physics*, 106(10):103509, 2009.
- [17] G. C. Sosso, S. Caravati, R. Mazzarello, and M. Bernasconi. *Physical Review B*, 83:134201, 2011.
- [18] E. Steigmeier and G. Harbeke. *Solid State Communications*, 8(16):1275 – 1279, 1970.

- [19] W. Richter and C. R. Becker. *Physica Status Solidi (b)*, 84(2):619–628, 1977.
- [20] M. Först, T. Dekorsy, C. Trappe, et al. *Applied Physics Letters*, 77(13):1964–1966, 2000.
- [21] E. Matsubara, S. Okada, T. Ichitsubo, et al. *Physical Review Letters*, 117:135501, 2016.

CONCLUSIONS

The renewed industrial interest in phase-change materials for integration in memory devices promoted intense research on this field, both from the engineering and the material physics point of view. Chalcogenide-based alloys can be switched back-and-forth between the stable amorphous and crystalline phases, via application of electrical/optical pulses of different time duration (fs to ns) and intensity. In this thesis, Ge-Sb-Te based nano-composites (of 2-D or 0-D dimension) have been studied in details. Here, we will directly address the Research Questions presented in Chapter 1.

Do “superlattice-like” GST materials represent a real challenging scenario with improved switching for future device technology?

Yes, but probably involving a complex process for phase-transition. Indeed, in Chapter 1 we have probed by means of EXAFS spectroscopy a representative 2-D highly-textured [GeTe (1 nm) / Sb₂Te₃ (3 nm)]₁₅ superlattice sample, determining its as-grown crystalline structure. We observed a slight compression of the Ge-Te bond lengths in the GeTe bilayers with respect to the nominal bulk values and an intermixing of Ge and Sb atoms at the interface between GeTe and Sb₂Te₃ building blocks. This study and the TEM investigation mutually support these remarks, tailoring the structural model of Ge-Sb-Te based superlattices. This knowledge is in fact pivotal to puzzle out a truthful representation of the possible phase-change mechanism in chalcogenide superlattices, which in principle should be more complex than just an atomic “umbrella”-flipping of Ge atoms in GeTe bilayers, as proposed in literature.

Does optical switching occur in 0-D GST materials? How do 0-D GST materials represent a valid alternative to higher-dimension counterparts in terms of energetics?

Yes, optical switching can occur in GST nanoparticles and the 0-D confinement effectively enhances the energy efficiency of the optical amorphisation, representing a valid alternative to higher dimension counterparts. We have proved the first crystalline-to-amorphous (RESET) transition in $\text{Ge}_2\text{Sb}_2\text{Te}_5$ nanoparticles of < 11 nm diameter with a single fs-laser pulse. XRD measurements validated the atomic structural disorder of the laser-induced state and its reversibility has been verified by Joule annealing above the crystallization temperature. Remarkably, we found an average amorphization threshold fluence of $< 1 \text{ mJ/cm}^2$, leading to a drop in energy cost for the RESET most consuming process, with respect to higher dimension $\text{Ge}_2\text{Sb}_2\text{Te}_5$ materials. In addition, we have shown that the Maxwell-Garnett theory -for modelling the optical response of granular media immersed in a dielectric matrix- well resembles the transmittivity of our system of a spherical nanoparticles layer with a 95 % coverage of the substrate. Finally, below threshold pump-probe (400 nm-800 nm) transmittivity measurements evidenced the existence of a photo-induced transient state lasting for few ps, before thermalization with lattice occur. The large agreement between data and theoretical simulations disclosed the resonant-bonding rupture as the origin of this metastable state. In addition, optical Raman-active phonons at ~ 3.7 THz -yielding Ge/Te atoms motion around their central position- slightly modulated the optical recovery.

In conclusion, we have assembled a thorough insight on structural and optical properties of two different kind of Ge-Sb-Te based nanoscaled phase-change materials, demonstrating the potentialities and advantages of following a dimensional reduction/-confinement strategy in optimizing the functionality of possible future technologies.

LIST OF PUBLICATIONS

- [1] R. Ciprian, F. Loi, E. Busetto, et al. *Review of Scientific Instruments*, 89(10): 105107, 2018.
- [2] B. Casarin, A. Caretta, B. Chen, et al. *Nanoscale*, 10:16574–16580, 2018.
- [3] G. Vinai, B. Ressel, P. Torelli, et al. *Nanoscale*, 10(3):1326–1336, 2018.
- [4] M. Malvestuto, R. Ciprian, A. Caretta, B. Casarin, and F. Parmigiani. *Journal of Physics: Condensed Matter*, 30(5):053002, 2018.
- [5] A. Caretta, M. Dell’Angela, Y.-D. Chuang, et al. *Physical Review B*, 96(18): 184420, 2017.
- [6] B. Casarin, A. Caretta, J. Momand, et al. *Scientific reports*, 6:22353, 2016.
- [7] R. Ciprian, P. Torelli, A. Giglia, et al. *RSC Advances*, 6(86):83399–83405, 2016.
- [8] A. Caretta, B. Casarin, P. Di Pietro, et al. *Physical Review B*, 94(4):045319, 2016.
- [9] M. Dell’Angela, F. Hieke, M. Malvestuto, et al. *Scientific reports*, 6:38796, 2016.
- [10] M. Malvestuto, A. Caretta, B. Casarin, et al. *Physical Review B*, 94(9):094310, 2016.
- [11] C. Svetina, N. Mahne, L. Raimondi, et al. *Journal of synchrotron radiation*, 23 (1):98–105, 2016.
- [12] J. Johannsen, G. Autès, A. Crepaldi, et al. *Physical Review B*, 91(20):201101, 2015.
- [13] B. Casarin, A. Cian, Z. Feng, et al. *The Journal of Physical Chemistry C*, 118 (12):6242–6250, 2014.

RINGRAZIAMENTI

Il mio primo ringraziamento va al **Prof. Parmigiani**, il mio supervisore nonché mentore in questi tre anni di percorso. La ringrazio per avermi dato l'opportunità di poter lavorare nel suo gruppo, per aver creduto nelle mie capacità e per avermi guidato seguendo da vicino tutte le mie scelte professionali. Grazie per i consigli, per il supporto e, non di meno, per tutti gli aneddoti raccontati che ricorderò sempre con affetto. Poi ovviamente vengono Marco e Toni. Questa tesi è decisamente anche vostra. **Marco**, non so se riuscirò mai a ringraziarti abbastanza per quello che hai fatto per me in questi anni. Da quando mi hai proposto di lavorare con te ne sono cambiate di cose. All'inizio ero timida, insicura e molto acerba nel lavoro: insomma hai creato un mostro! A parte gli scherzi, se sono cresciuta nel modo di avvicinarmi alla ricerca, ad appassionarmi, ad insistere fino ad ottenere il risultato è soprattutto grazie a te. Mi hai fin da subito dato delle responsabilità a cui non credevo di poter far fronte. Mi hai fatto capire che nella fossa dei leoni bisogna saperci stare e non aver paura di affrontare le critiche, anzi di essere sempre preparati. Grazie a te ho viaggiato tantissimo, ho conosciuto molte persone. Con la tua calma mi hai insegnato ad aver pazienza, tanta pazienza, anche se delle volte alla fine istigavo io te! Insomma, tutto questo per dirti che sai che basta un fischio e una soppresa e un prosecco te li porterò sempre, perché posso anche andare avanti ma non dimenticherò mai da dove e con chi ho iniziato.

Ah **Toni**, adesso tocca a te! Te l'avrò ripetuto già circa un milione e mezzo di volte, ma scritto nero su bianco e in maiuscolo fa un effetto diverso: GRAZIE! Grazie perché senza di te in questi anni sarei stata persa. Mi hai insegnato tante di quelle cose che solo ad elencarle ci metterei un altro anno di dottorato! Grazie perché hai avuto la pazienza di rispondere ripetutamente a tutte le mie domande e ad avermi dato la libertà di fare (e di sbagliare) in laboratorio, tanto eri sempre lì pronto a venire in aiuto! La prima persona che interpellavo per qualsiasi cosa eri tu. Grazie perché la tua

infinita curiosità e la grande passione che metti nel lavoro mi hanno sempre ispirata. Grazie per avermi fatto sentire il tuo “braccio destro”, per avermi trattato da “persona pensante” e non solo da mera esecutrice di ordini. Sono contentissima di tutto quello che abbiamo costruito e portato a termine insieme. E parlo anche del rapporto di amicizia e stima che mi lega a te. È incredibile quante risate ci siamo fatti. L'allegria è stata una costante di questi tre anni, e non posso che ricordarlo con nostalgia. Non sei mai riuscito a convertirmi all'arrampicata quindi non riuscirò a venirti a trovare in qualsivoglia parete, ma sono sicura che per portarti giù basterà corromperti con una birretta!

Grazie a **Roberta**. Sono felice di poter dire di aver lavorato con te. Di averti potuta affiancare e di aver potuto “rubare con gli occhi” ogni tua più piccola mossa. Da come approcciarsi con i collaboratori, a come darsi da fare e trovare sempre alternative quando si hanno le spalle al muro. Grazie per le pause che mi costringevi a fare, di cui sapevi benissimo avevo bisogno. Da quando te ne sei andata, è stato difficile. Avrei voluto festeggiare con te la fine di questo percorso, ma sono sicura che comunque -dovunque tu sia- sarai orgogliosa di come ho portato avanti le cose. E credimi, porterò te, il tuo sorriso e la tua determinazione sempre con me.

Poi vengono i miei genitori, **Luciano** e **Giovanna**. Grazie perché nonostante -prima l'università e poi il dottorato- mi abbiano portato (un po') distante da casa, avete sempre accettato e supportato ogni mia scelta professionale. Quando vi ho detto che avevo bisogno di uno spazio mio, mi avete aiutato a crearlo dal nulla. E quando ho capito che volevo provare altre strade, siete stati i primi ad incoraggiarmi. Quando ho bisogno di qualsiasi cosa ci siete. Non potrei essere più fortunata di così. Grazie mamma e papà!

Vale. Per te davvero è difficile trovare le parole. Grazie per essere la mia migliore amica, la mia prima confidente, il mio sostegno e la mia parte lucida quando mi faccio prendere dall'ansia. Grazie per non aver mai permesso che mollassi un colpo, per avermi fatto ragionare e vedere le cose da una prospettiva sempre nuova. Grazie a te e grazie a **Marco** perché le vostre esperienze e i vostri consigli mirati e spassionati sono sempre stati un faro per me in questi anni di dottorato. E grazie ancora a voi perché con l'arrivo di Ricky mi avete regalato una gioia immensa a cui non riesco a stare distante.

Grazie alla mia **ciurma**, che anche se distante era sempre lì. Grazie alle mie amiche di sempre, **Sara, Rachele, Carlotta, Chiara e Serena**. Quasi trent'anni insieme sono tanti, vi chiedo scusa per le mie assenze e vi ringrazio per aver trovato comunque il tempo per condividere la vostra vita con me. In questi tre anni, sapere di poter contare su di voi (per divertirci, chiaccherare o per sfogarci e consigliarci) mi ha sempre dato coraggio.

Grazie ai miei amici/colleghi triestini-ma-neanche-tanto **Andrea, Giulia, Martina, Franz, Francesca, Giorgia e Luca**. Mi macheranno gli aperitivi, le cene e i rebechin a base regionale che si facevano per uscire un po' da questa "baita"!

E infine *-last but not least-* grazie **Manuel**. Ci siamo conosciuti poco prima di intraprendere questa avventura. Hai vissuto con me tutti gli alti (pochi) e bassi (molti) di questo percorso. Hai sopportato le mie indecisioni, le insicurezze, le arrabbature ma anche le piccole grandi vittorie e soddisfazioni che ho avuto. Grazie per essermi stato e per starmi ancora accanto. Grazie per essere cresciuto insieme a me, personalmente e professionalmente. Anche se hai capito un decimo di quello che ti raccontavo, mi hai donato il tuo supporto incondizionato e hai saputo consigliarmi per il mio bene. Grazie per avermi fatto svagare. E grazie allo stesso tempo aver compreso e accettato la mia assenza quando ero in laboratorio o durante i beamtime. Sono stati tre anni intensi ma ce l'abbiamo fatta, e adesso scopriremo insieme cosa ci riserva il futuro.

Mi scuso per questi ringraziamenti molto informali, ma li ho scritti di getto e chi mi conosce sa bene che rappresentano esattamente la persona che sono.